

6

3772

3773

3774

Improved RPC investigation and preliminary electronics studies

3775 The extension in the endcap of the RPC sub-system towards higher pseudo-rapidity will bring the
3776 new detectors to be exposed to much more intense background radiations due to the proximity of
3777 the detectors with the beam line (Figure 4.5). The challenge will be to produce high counting rate
3778 detectors with limited ageing rate to ensure a stable operation of the detector over a period longer
3779 than ten years. In Chapter 3 was discussed the influence of the detector design (number and thickness
3780 of gas volumes, OR system, etc...) on the charge deposition and rate capability. Nevertheless, this
3781 question can also be addressed from the electronics point of view as a better signal-to-noise ratio
3782 would also mean the possibility to greatly lower the charge threshold on the signals to be detected,
3783 allowing to use the detector at lower gain, hence lowering the charge deposition per avalanche in the
3784 gas volume. Cardarelli showed that the production of low-noise fast FEEs could help decreasing the
3785 charge deposition per avalanche at working voltage by an order of magnitude, virtually increasing
3786 the life expectancy of such a detector in the same way [281].

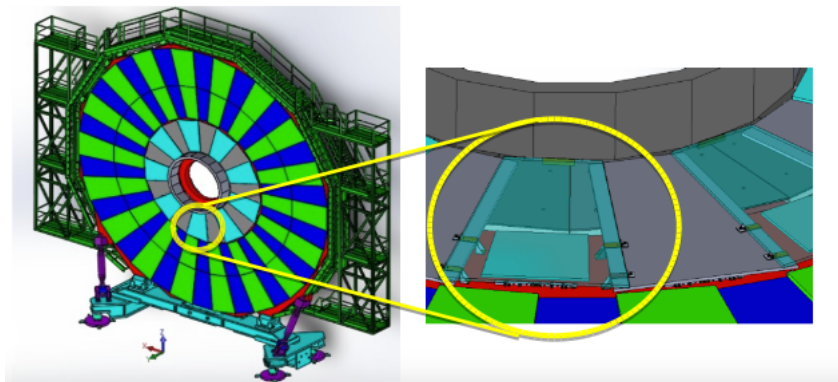
3787 In this Chapter will be presented the electronics that were chosen to equip the iRPCs that will
3788 installed on the CMS endcaps at the positions RE3/1 and RE4/1. These electronics are the CMS
3789 RPCROC. A similar technology has been previously used with RPCs in the context of the R&D of a
3790 Semi-Digital HCAL (SDHCAL) for the International Large Detector (ILD). As back-up to the CMS
3791 RPCROC, a FEB developed by the INFN Tor Vergata in Rome as also been studied for the CMS
3792 iRPCs.

3793 These two solutions for the iRPCs are the results of a longer selection process in which I took a great
3794 part. Thus, after an introduction of both technologies, the tests performed on CMS RPCs operated
3795 with preliminary versions of INFN Tor Vergata preamplifiers as well as with the HARDROC 2
3796 read-out panel of the SDHCAL will be discussed in details. Finally, the current status of the R&D
3797 certification will be presented. Nonetheless, it is important to keep in mind that I did not personally
3798 participate in the development of the CMS RPCROC nor of the INFN Tor Vergata FEB as designed
3799 for the iRPCs. My role was limited to the selection and to the test of potential candidates. After
3800 this preliminary study was conducted, the development of the actual FEEs for the CMS iRPCs was
3801 conducted by other researchers. Therefore, I will only report the status of the ongoing research.

3802 6.1 FEE candidates for the production of iRPCs

3803 The extension of the third and fourth endcap disks with improved RPCs has been presented in
 3804 Chapter 4 together with the expected background levels (Figure 4.18). The iRPCs will complete the
 3805 muon endcap as described in Figure 6.1. The key features of these iRPCs are:

- 3806 • double-gap design,
- 3807 • 1.4 mm thick HPL electrodes,
- 3808 • 1.4 mm thick gas gap,
- 3809 • trapezoidal chambers spanning 20° in φ around the beam axis,
- 3810 • read-out panel consisting of 96 trapezoidal strips
- 3811 • strip pitch ranges from 6.0 mm (5.9 mm) on the high pseudo-rapidity end to 12.3 mm (10.9 mm)
 3812 on the low one on position RE3/1 (RE4/1)
- 3813 • spatial resolution in the direction perpendicular to the strips ~ 3 mm



3814 *Figure 6.1: Location of the RE3/1 or RE4/1 iRPCs on a muon endcap disk.*

3815 An important piece of these iRPCs will be the Front-End Electronics that will equip the chambers.
 3816 A fast, low-jitter and low-charge sensitive electronics will help reducing further the charge
 3817 deposition in the detector by making it possible to operate at lower gain. The FEEs that are foreseen
 3818 to equip the new RPCs need to be able to detect charges as small as 10 fC. Not only the new elec-
 3819 tronics need to be fast and reliable, they also should be able to sustain the high radiation the detectors
 will be subjected to in the region closest to the beam.

3820 6.1.1 CMS RPCROC: the RPC upgrade baseline

3821 Designed by Weeroc, a spin-off company from the OMEGA Collaboration, the PETIROC 2A consists
 3822 in a fast and low jitter 32-channel ASIC originally developed to read-out Silicon Photomultiplier
 3823 (SiPM) in ToF applications and that allows for precise time measurements [257, 258]. The ASIC
 3824 uses an AMS 350 ns Silicon-Germanium (SiGe) technology. The block diagram of the ASIC is
 3825 showed on Figure 6.2. A 10-bit DAC allows to adjust the trigger level in a dynamical range spanning
 3826 from 0.5 to a few tens of photoelectrons and a 6-bit DAC to adjust the response of each individual
 3827 channel to similar a level.

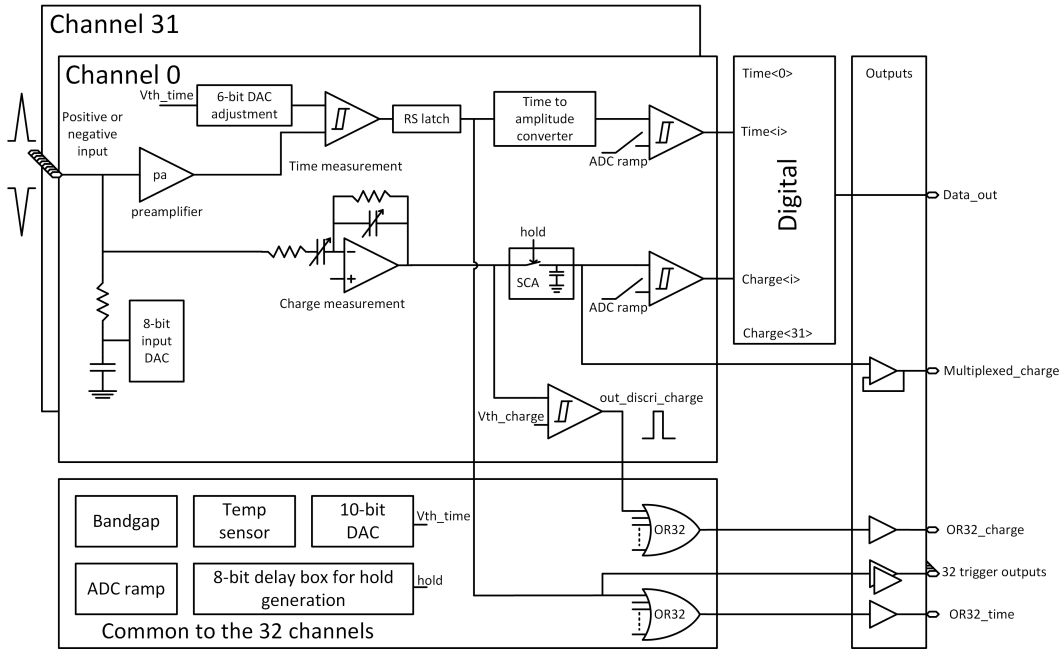


Figure 6.2: PETIROC 2A block diagram.

Nevertheless, to adapt this ASIC to CMS, modifications were brought to the PETIROC [177] and not all its functions will be used [282]. Due to the radiation levels that are foreseen at the level of the iRPCs, the SiGe technology will be replaced by the Taiwan Semiconductor Manufacturing Company (TSMC) 130 nm CMOS, to increase its radiation hardness while keeping fast pre-amplification and discrimination. On the Front-End Board, the ASIC is associated with an FPGA which purpose is to measure the arrival time of the signals. The FPGA is equipped with a TDC with a time resolution of 50-100 ps developed by Tsinghua University. The full system will provide a measurement of the signal position along the strip with a precision of a few cm by reading the signal on both strip ends. Finally, the measurement of the charge will be performed by a Time-over-Threshold (ToT) technic, taking profit of the capacity the ASIC in measuring both the leading and trailing edges of the input signals.

Two consecutive versions of the RPCROC are showed in Figure 6.4. FEBv0 was equipped with a single PETIROC 2A associated to a Cyclone II FPGA and the FEBv1 with two PETIROC 2A associated to a Cyclone V FPGA. The next version, the FEBv2 is expected to be equipped with three PETIROC 2C, the new generation of the ASIC, associated to three Cyclone V FPGAs hosting the 32-channel TDCs and a master Cyclone V FPGA for the communications of the TDCs with the Link-Board system. The PETIROC 2B was a version of the ASIC with less cross-talk than the 2A. The dynamic range could then be expanded towards lower values to allow for the detection of charges as low as 50 fC. The version 2C will focus on reducing the dead-time of 10 ns of the ASIC. Also, the Cyclone V FPGAs of the FEBv2 will use a different technology than the one used for FEBv1. The choice has been made to use a radiation tolerant PolarFire FPGA which uses data scrubbing to detect and correct errors before they accumulate. This technology is for example used for space applications. The FEB will be tested at the Louvain-la-Neuve (LLN) neutron beam. The goal is to irradiate the electronics up to a fluence of 10^{14} pC/cm^2 , five times more than what is expected at CMS, to certify its radiation hardness.

3853



Figure 6.3: (a) View of the RPCROC FEBv0 in which the PETIROC 2A ASIC is visible as well as the FPGA on which the TDC is hosted. (b) View of the RPCROC FEBv1 with its two PETIROC 2A ASICs. The FPGA with the TDC is this time embeded in the FEB.

3854 Each FEBv2 will be able to read 96 channels out thanks to three 32-channel PETIROC 2C
 3855 ASICS. Two FEBv2 would be mounted on the iRPC to read the 96 strips out from both ends. The
 3856 read-out panel that was used for the v1 of the RPCROC is shown in Figure 6.4a and the final design
 3857 with the FEBv2 mounted on the read-out plane is shown in Figure 6.4b.

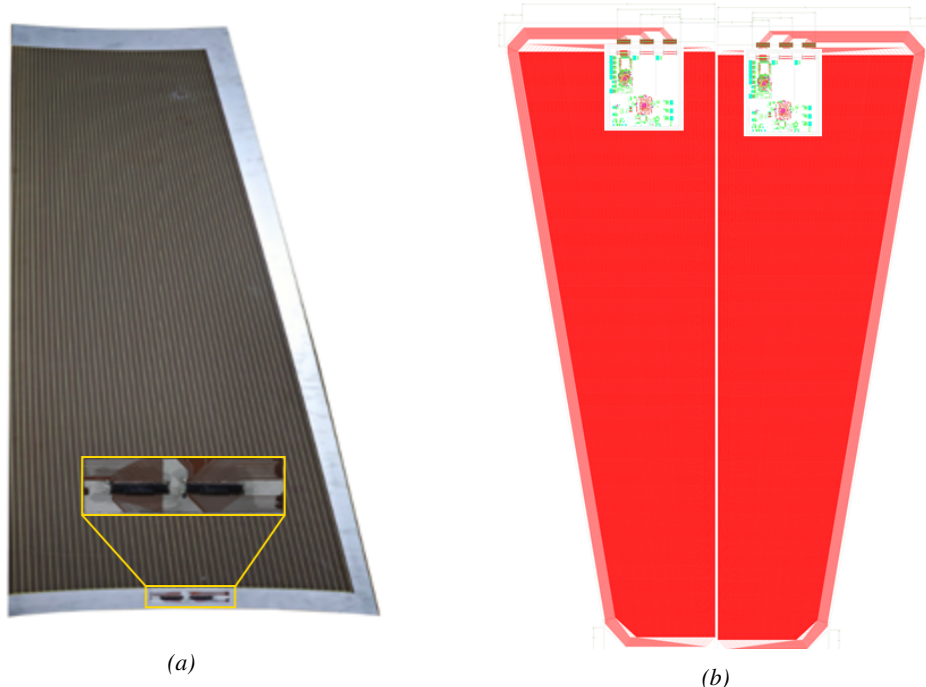


Figure 6.4: (a) Picture of half the read-out PCB used with FEBv1. The RPCROC is connected directly onto the return connectors on the wide end of the panel. (b) Design of the foreseen final read-out of the iRPC showing the 2 RPCROC FEBs and the read-out PCB.

3858 **6.1.2 INFN FEB: a robust back-up solution**

3859 Even though the baseline for the electronics that will equip the iRPCs will be the CMS RPCROC,
 3860 a back-up solution needs to be certified. The back-up has been found in Front-End Electronics
 3861 featuring a fast and low-noise ($1000 e^-$ rms) Silicon (Si) preamplifier and a SiGe discriminator [283]
 3862 associated with an optimized read-out panel [284]. The low-noise preamplifier is a new version of
 3863 a preliminary production of a SiGe preamplifier by the team of Cardarelli working with INFN Tor
 3864 Vergata in Rome with the purpose of equipping the new generation of ATLAS RPCs [285]. The
 3865 study of the early version of the preamplifier by is discussed in Section 6.2.

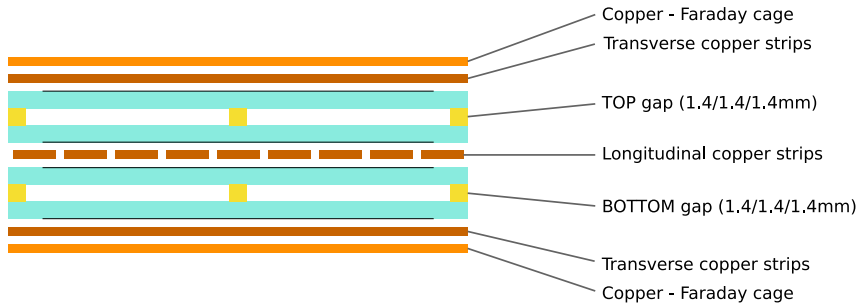


Figure 6.5: Design of the iRPC in the back-up scenario. The detector includes an additional two layers of transversal strips to gain in spatial resolution.

3866 Contrary to the CMS RPCROC, the back-up electronics only offer the possibility to read the
 3867 96 strips out from one end. The spatial resolution along the strips is then brought by two transverse
 3868 strip planes. These two additional panels sandwich the *gaps+strip* ensemble as showed in Figure 6.5.
 3869 They feature 5 cm wide copper strips for a spatial resolution of a few centimeters along the longitudi-
 3870 nal strips. A top quarter of the longitudinal and transversal read-out panels is shown in Figure 6.6
 3871 and pictures are available in Figure 6.7.

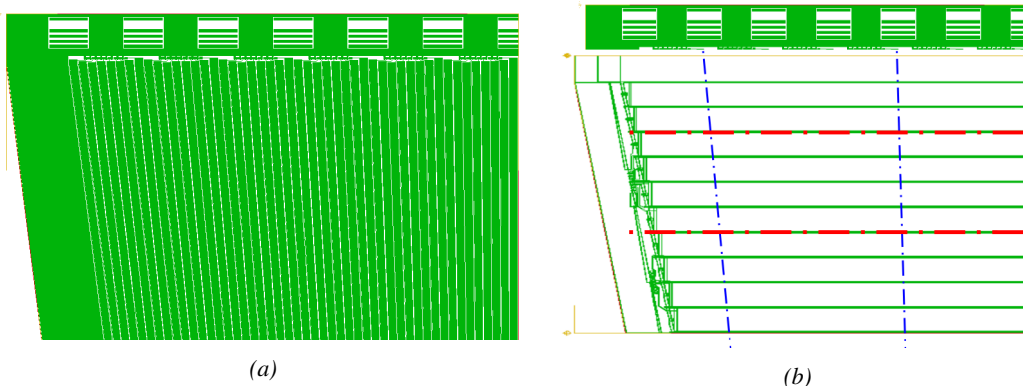


Figure 6.6: Design of the longitudinal (a) and transversal (b) strip panels. The transversal design is here shown on top of the longitudinal one.

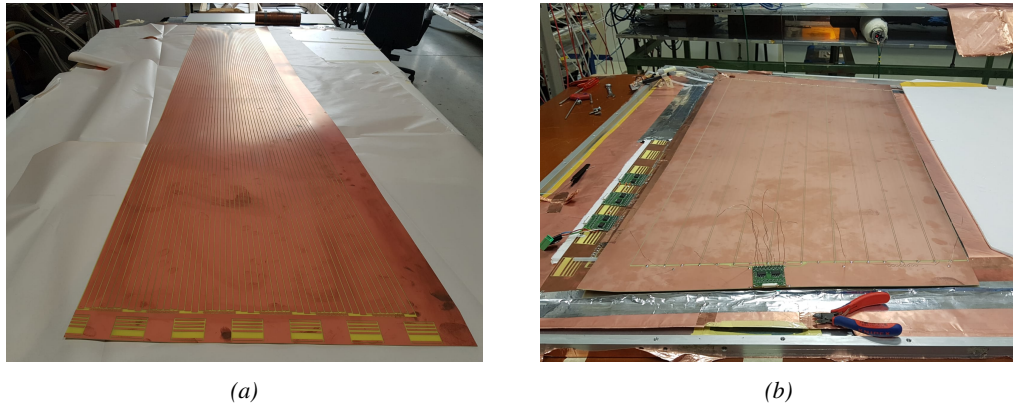


Figure 6.7: Picture of half the longitudinal (a) and of the top part of the transversal (b) strip panels.

3872 The FEB used for the longitudinal readout is shown in Figure 6.8a. Each FEB is equipped
 3873 with eight preamplifiers using a Bipolar Junction Transistor (BJT) technology and two discriminator
 3874 ASICs of four channels using Hetero Junction bipolar Transistor (HJT) technology. The input
 3875 signals are amplified at an amplification factor of 0.2 to 0.4 mV/fC and are then discriminated with
 3876 a threshold of 0.5 mV at minimum. For each channel, the LVDS output is proportional in width to
 3877 the Time-over-Threshold in the discriminator of the amplified signal with a minimum width of 3 ns.
 3878 This method allows for an estimation of the avalanche charge as the width of the signals usually is
 3879 consistent and proportionnal to the amount of charge released in the gas volume.
 3880 On Figure 6.6a, the rectangular zones with straight copper lines at the top of the longitudinal PCB
 3881 are lines used to propagate the power and the slow control of the FEBs. A FEB is placed between
 3882 two zones and soldered to the copper lines on both sides, as can be seen in Figure 6.8b. in the same
 3883 way, the FEB is soldered to a group of eight strips which lines finish into pads placed below the
 3884 bottom edge of the FEB. It was decided to solder the FEBs onto the read-out PCB to reduce the
 3885 pick-up noise in the electronics.

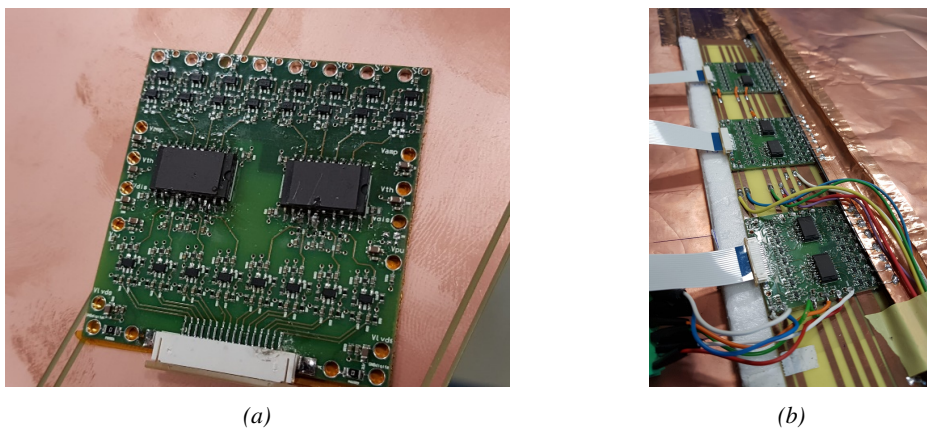


Figure 6.8: Version 2 of the INFN Tor Vergata FEB as designed for the CMS iRPC. The FEBs are directly soldered onto the read-out PCB to reduce pick-up noise as much as possible. Copper lines embedded into the PCB are used to propagate the power and slow control lines.

3886 The strips begin much wider in the case of the transversal read-out panel, the FEB design is a

3887 little different, as can be seen in Figure 6.9a. The transversal FEBs are strictly the same as the one
 3888 attached to the longitudinal plane even though they are wider. AS of now, the connection of the
 3889 FEBs to the power and slow control lines is done via coaxial cables as can be seen from Figure 6.9b.
 3890 Only the connection to the strips was optimized for direct on-PCB soldering.

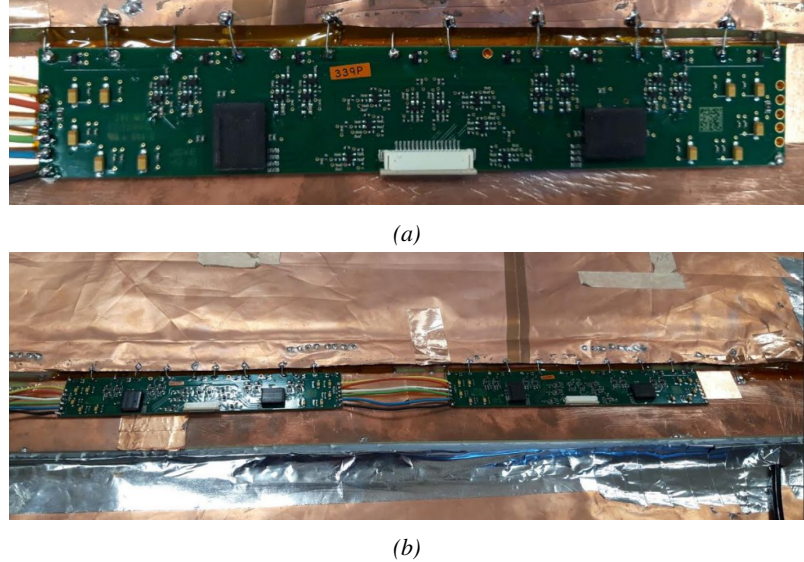


Figure 6.9: Version of the INFN Tor Vergata FEB as designed for the transversal readout panels of the CMS iRPC. The FEBs are directly soldered onto the read-out PCB to reduce pick-up noise as much as possible. The propagation of the power and slow control lines is done via coaxial cables.

3891 6.2 Preliminary electronics tests at CERN

3892 6.2.1 INFN preamplifiers as upgrade candidates

3893 INFN electronics were the first ones to be
 3894 tested by CMS RPC group in collaboration
 3895 with colleagues from INFN Roma working in
 3896 the ATLAS RPC group. The tests with CMS
 3897 RPCs were performed in February 2013 out-
 3898 side of the old GIF facility presented in Chap-
 3899 ter 5.1.1. Four preamplifier channels were
 3900 lended by Cardarelli to equip four CMS RPC
 3901 channels as presented in Figure 6.13. They
 3902 were directly connected to the strips for the
 3903 signals induced by muons passing through the
 3904 gas volume of the chamber to be amplified.
 3905 The output was then sent to a discriminator
 3906 to digitize the signals and filter out the noise
 3907 by tuning the threshold level. The NIM quad
 3908 discriminator 821 manufactured by LECROY
 3909 used during this experiment only allows at minimum to set the threshold at a voltage of approxi-
 3910 mately 30 mV on the input signals. Thus, two values of discrimination were used (~ 75 mV and

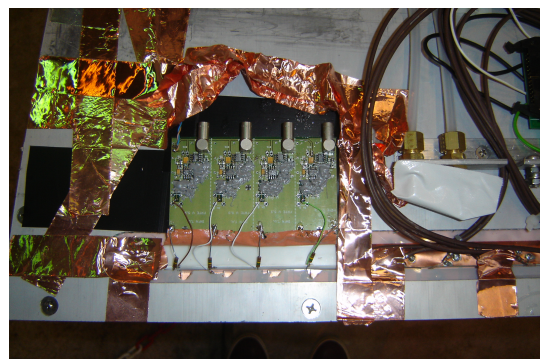


Figure 6.10: The four channels of INFN preamplifiers are mounted directly on a CMS RPC and connected to the four outermost read-out strips of the detector.

³⁹¹¹ ~ 30 mV).

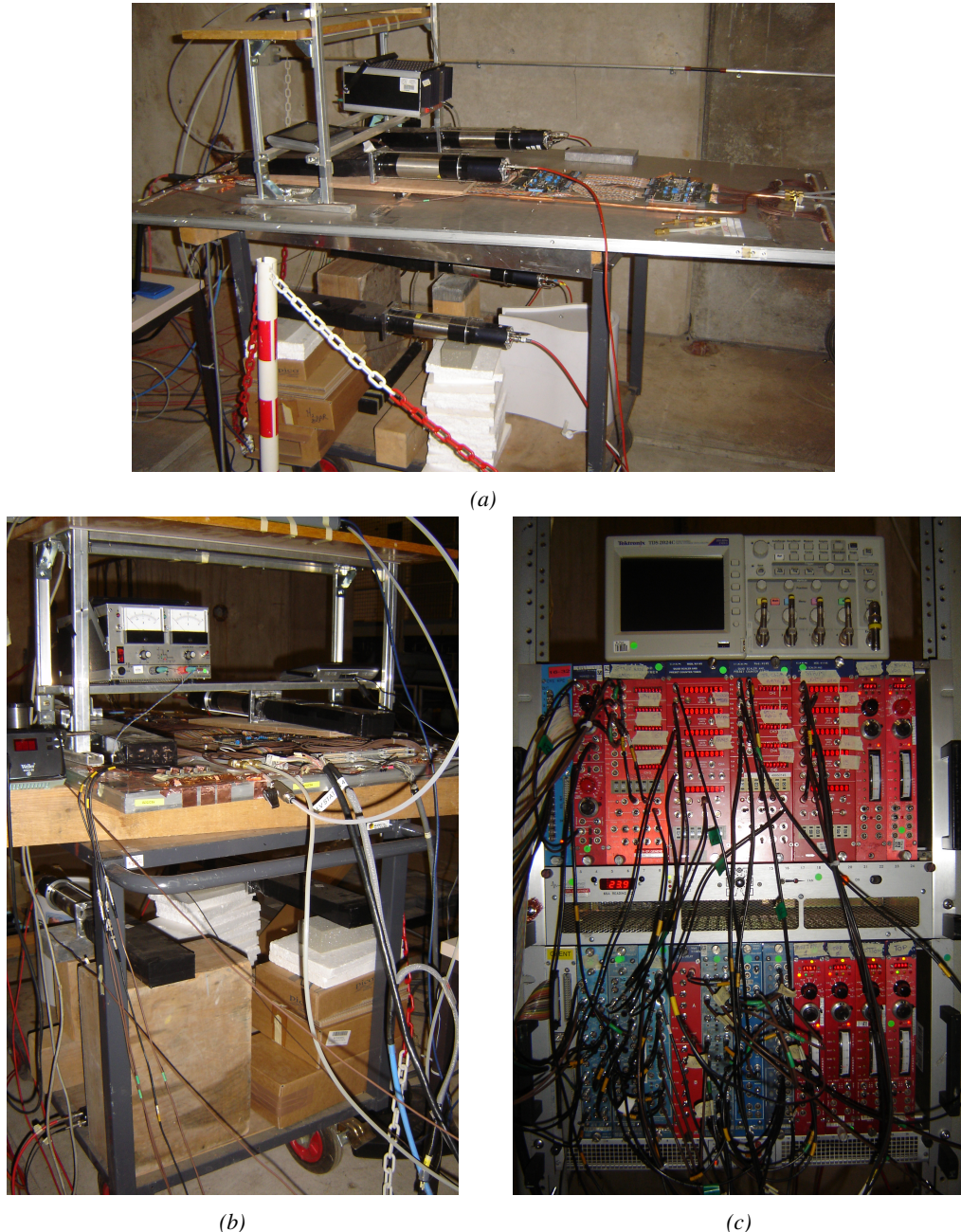


Figure 6.11: Experimental setup used to test the INFN preamplifier with respect to the CMS FEEs.

³⁹¹² The performance of the chamber equipped with these new preamplifiers was compared to the
³⁹¹³ performance of CMS FEEs. The experimental setup used is described in Figure 6.11. PMTs a little
³⁹¹⁴ less wide than four strips were used to trigger the data taking. Two pairs were used in coincidence
³⁹¹⁵ on both the strips connected to the INFN preamplifiers and to the ones connected to the CMS FEEs.

3916 An extra PMT, placed perpendicularly to the rest of the setup at the bottom of the setup was used
 3917 to detect potential showers and send VETO signals if necessary. A last PMT was used close to the
 3918 power supplies to measure and discard signals due to electromagnetic noise and is not visible on
 3919 the pictures. Finally, after discrimination, the output of the INFN preamplifiers together with the
 3920 signals from the CMS FEEs were sent to scalers to count the detected signals versus the number of
 3921 trigger coincidences as no DAQ software was available at the time. The full pulse processing for this
 3922 experiment is shown in Figure 6.12.

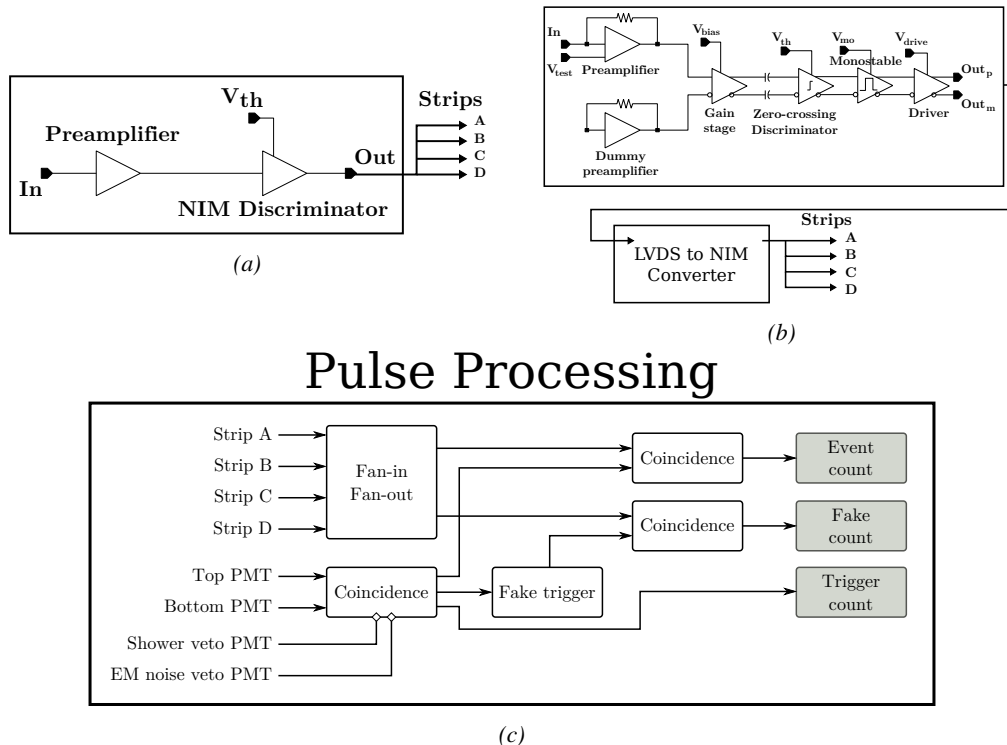


Figure 6.12: The block diagrams corresponding to the signal treatment for both INFN preamplifier (Figure 6.12a) and CMS FEEs (Figure 6.12b) are shown. The digitized signals are then counted in coincidence with the trigger signals provided by PMTs (Figure 6.12c).

3923 The data taking program consisted in High Voltage scans. A first point was taken at 0 V to only
 3924 measure noise. Then the HV was increased to an applied value of 7 kV. The voltage was increased
 3925 in steps of 500 V until 8 kV from where it was increased in steps of 100 V until an upper limit of
 3926 10 kV. After rising the voltage over the electrodes of the RPC, a waiting period of 15 minutes was
 3927 observed to leave time to the electrodes to charge and to the currents to stabilize. The currents were
 3928 reported at the moment the data taking was started. At each HV step, except at 0 V, approximatively
 3929 300 triggers were taken to estimate the efficiency of the detector by counting the number of hits in
 3930 the system (A or B or C or D), referring to the strips. The noise rate per unit area was measured dur-
 3931 ing the first 100 s of data taking by counting the number of hits received in each read-out strip. The
 3932 cluster size, the average number of adjacent strips fired during a muon event, could not be measured
 3933 due to the lack of available scalers.
 3934 During the data acquisition, in addition to counting the number of signals with respect to the number
 3935 of triggers, the current or the noise rate per unit area as a function of the increasing voltage, the
 3936 environmental parameters were monitored. Using the information provided by a humidity and tem-

perature sensor on the gas input line together with the environmental pressure given by a weather station, the applied voltage could be corrected following Formula 3.27. Moreover, the voltage line was filtered to prevent noise and higher currents in the RPC under test.

The results of the preliminary tests are presented in Figure 6.13. More details on the fit performed on the data are provided in Table 6.1. As can be seen, being able to use electronics with a much higher sensitivity allows for a HV shift of up to 475 V with a threshold as low as 3 fC corresponding to the lowest threshold available on the discriminator modules. On the other hand, the higher charge sensitivity also brings a higher noise level. After a first series of measurement performed with a bad grounding leading to grounding loops and hence an artificially higher noise, it can be concluded that the noise rate per unit area of such electronics is approximately one of manitude higher than the noise rate measured with the CMS FEB. The noise reaches approximately 2 Hz/cm^2 at the level of the working in the case of the INFN preamplifier while it is lower than 0.2 Hz/cm^2 for the CMS FEB. It is likely that the higher sensitivity also brings a higher sensitivity to local discharges happening in the gas due to fluctuations of the electric field. The surface of the electrodes not being perfectly smooth, the local electric field may vary quickly. The gas molecules circulating in the gas could then be ionised by the fast variation of the field and trigger an avalanche that can then be detected. Reducing the noise rate per unit area would then come from an improvement of the detector itself rather than from a reduction of the electronic noise of the INFN preamplifier.

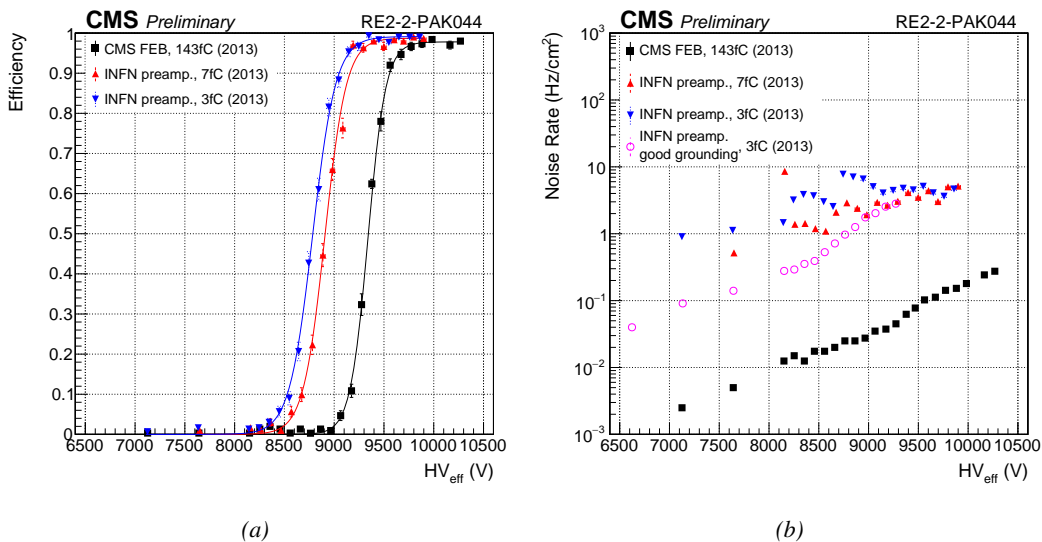


Figure 6.13: Efficiency (Figure 6.13a) and noise rate per unit area (Figure 6.13b) of the CMS RE2-2 detector tested with the standard CMS FEBs (black) and with the INFN preamplifier at different thresholds (red and blue). An extra HV scan was performed with better conditions to measure the noise with a threshold of 3 fC on the INFN preamplifiers.

Data	ϵ_{max}	$\lambda (\times 10^{-2} \text{ V}^{-1})$	$HV_{50} (\text{V})$	ϵ_{WP}	$HV_{WP} (\text{V})$
CMS FEB, 143fC (2013)	0.978 ± 0.004	1.12 ± 0.07	9339 ± 11	0.97 ± 0.01	9752 ± 27
INFN preamp., 7fC (2013)	0.987 ± 0.003	0.93 ± 0.05	8907 ± 11	0.97 ± 0.01	9374 ± 27
INFN preamp., 3fC (2013)	0.991 ± 0.003	0.86 ± 0.04	8783 ± 11	0.98 ± 0.01	9276 ± 27

Table 6.1: Results of the sigmoid fit (Formula 3.24) performed on the data presented in Figure 6.13a. The working point and its corresponding efficiency are computed using Formulas 3.24 and 3.25.

3955 6.2.2 INFN preamplifiers mounted onto CMS Front-End Board

3956 Following the first experiment performed in the experimental hall aside of the old GIF, a new se-
 3957 ries of tests has been done in the CMS RPC assembly laboratory at CERN. For this purpose, the
 3958 preamplifiers have been designed to be standalone single channels. To have a consistent comparison
 3959 with the CMS FEB, a FEB prototype has been built based on the current CMS design. As shown
 3960 in Figure 6.14, the preamplifiers are meant to be plugged in one of the available 16 channels of the
 3961 board that produces an LVDS output with similar characteristics than the CMS FEB.

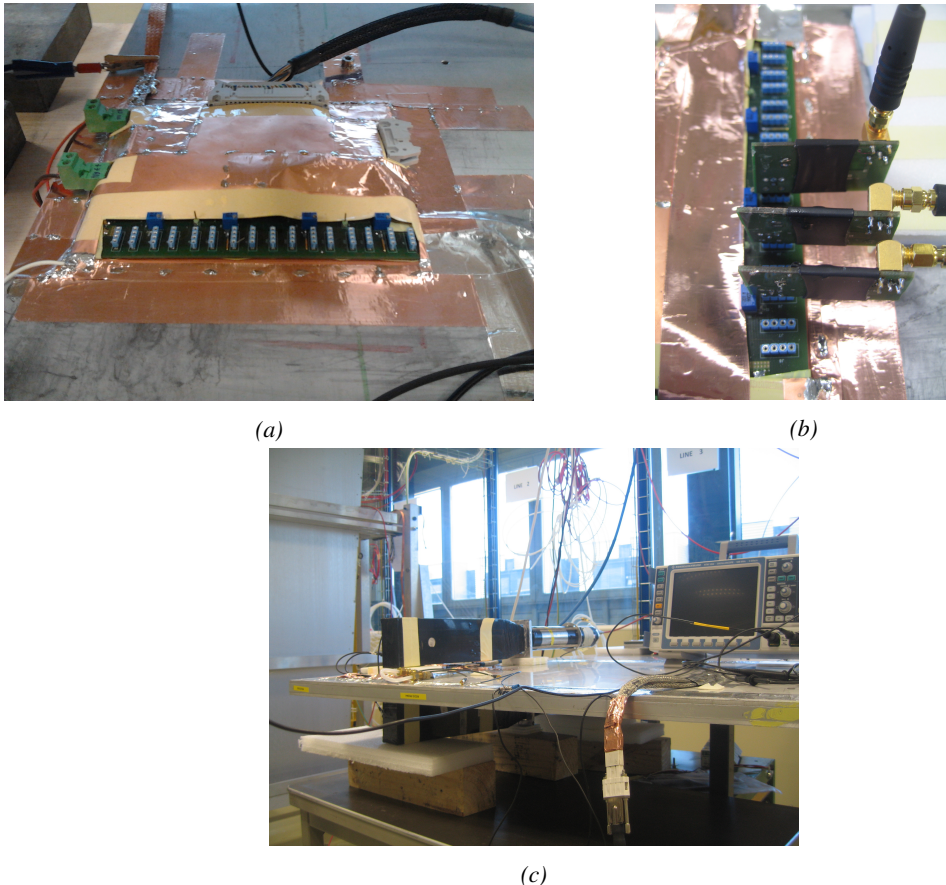


Figure 6.14: Figure reffig:Setup-INFN-904:A: Shielded Front-End Board on which the INFN preamplifiers are to be mounted. Figure reffig:Setup-INFN-904:B: Three INFN preamplifiers connected onto the test FEB. Figure reffig:Setup-INFN-904:C: Experimental setup used to test the INFN preamplifier single mounted on a FEB similar to the CMS FEB.

3962 At the time of the second experiment, only three channels could be lended by the team of INFN
 3963 Roma. The impedance of the preamplifiers was set to 100Ω at delivery. The strips are then con-
 3964 nected to the preamplifiers using 50Ω coaxial cables equipped with SMC connectors, known for
 3965 their good transmission. To match the impedance of the preamplifier input with the signal cable,
 3966 a 100Ω resistor was added in parallel of the input line. In CMS endcap RPCs, the strips are left
 3967 floating. For the purpose of this test, it was necessary to terminate the strips on both ends to prevent
 3968 reflections in the transmission line. The impedance of the strips being approximately 25Ω , the strips
 3969 were terminated with 50Ω resistors on the signal cable side, and with 25Ω resistors on the end side.

3970 The threshold of the zero-crossing discriminators used on the FEB is controled via a labview interface
 3971 similar to the one used to control the threshold of the CMS FEB. Various thresholds were used
 3972 in a range in between 7 and 5 fC. These values are a little higher than the minimal threshold of about
 3973 3 fC used during the first experiment due to limitations of the FEB itself.

3974 Finally, it was decided to use the same PMTs than in the first experiment as trigger. This time, they
 3975 were placed on their narrow side to only cover an area on the detector smaller than three strips. On
 3976 the data acquisition side, no DAQ software was available yet at the time of experimentation and
 3977 scalers were once again used. As can be seen from Figure 6.15, the pulse processing has been in-
 3978 spired by the previous scheme. Thanks to the lower number of channels to monitor, the cluster size
 3979 could be estimated by counting the signals on single channels (A, B and C on their own) but also
 3980 on groups of two (A and B, B and C) and three channels (A and B and C) in coincidence with the
 3981 trigger.

Pulse Processing

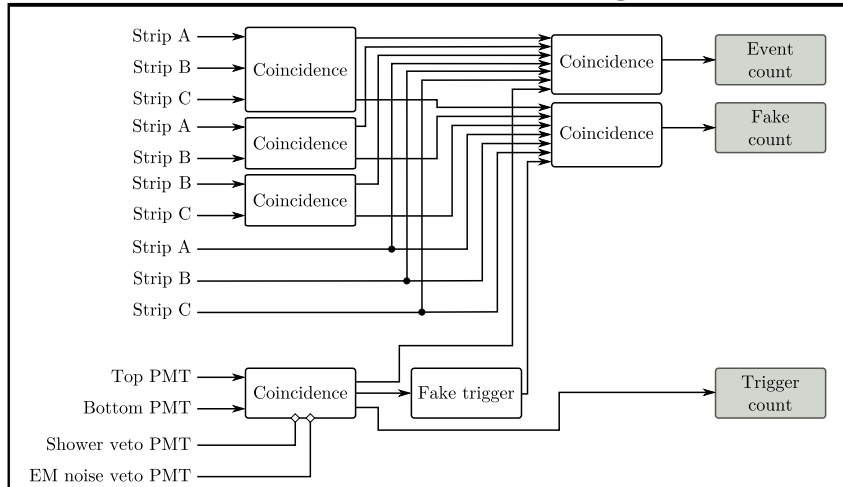


Figure 6.15: Similarly to Figure 6.12c, the signals are counted in coincidence with the trigger signals provided by PMTs. To estimate the cluster size, the channels are counted by groups of three, two but also alone.

3982 The results of the second round of tests with INFN preamplifiers are presented in Figure 6.16 and
 3983 Table 6.2. These results are consistent with what was measured with the first tested prototypes. The
 3984 efficiency sigmoid has been measured once again with the CMS FEB, using a threshold of 146 fC
 3985 and is in agreement with the data collected in 2013. The performance of the detector with the pream-
 3986 plifiers tuned at 7.2 and 6.4 fC falls in the very same values than the setting at 7 fC according to the
 3987 table. A maximum shift of 410 V is observed for a threshold of 5 fC.

3988 With the care placed into having a good grounding of the setup as well as a good impedance match-
 3989 ing, the noise rate per unit area is this time lower than what previously measured. Nevertheless, it
 3990 still is more than one order of magnitude higher than in the case of the CMS FEB with a threshold
 3991 set at 146 fC. The noise rate is measured to be at lowest around 0.7 Hz/cm^2 when measured to be
 3992 approximately 0.05 Hz/cm^2 for the CMS FEB. At such high threshold values, the noise rate per unit
 3993 area is not expected to vary much. The data collected at the RPC assembly laboratory then displays
 3994 much better data tacking conditions with both electronics.

3995 Finally, the cluster size is measured to be similar for both electronics at the level of the working
 3996 point and is in between 2.2 and 2.4 strips on average. The spatial resolution of both devices would
 3997 then be the same.

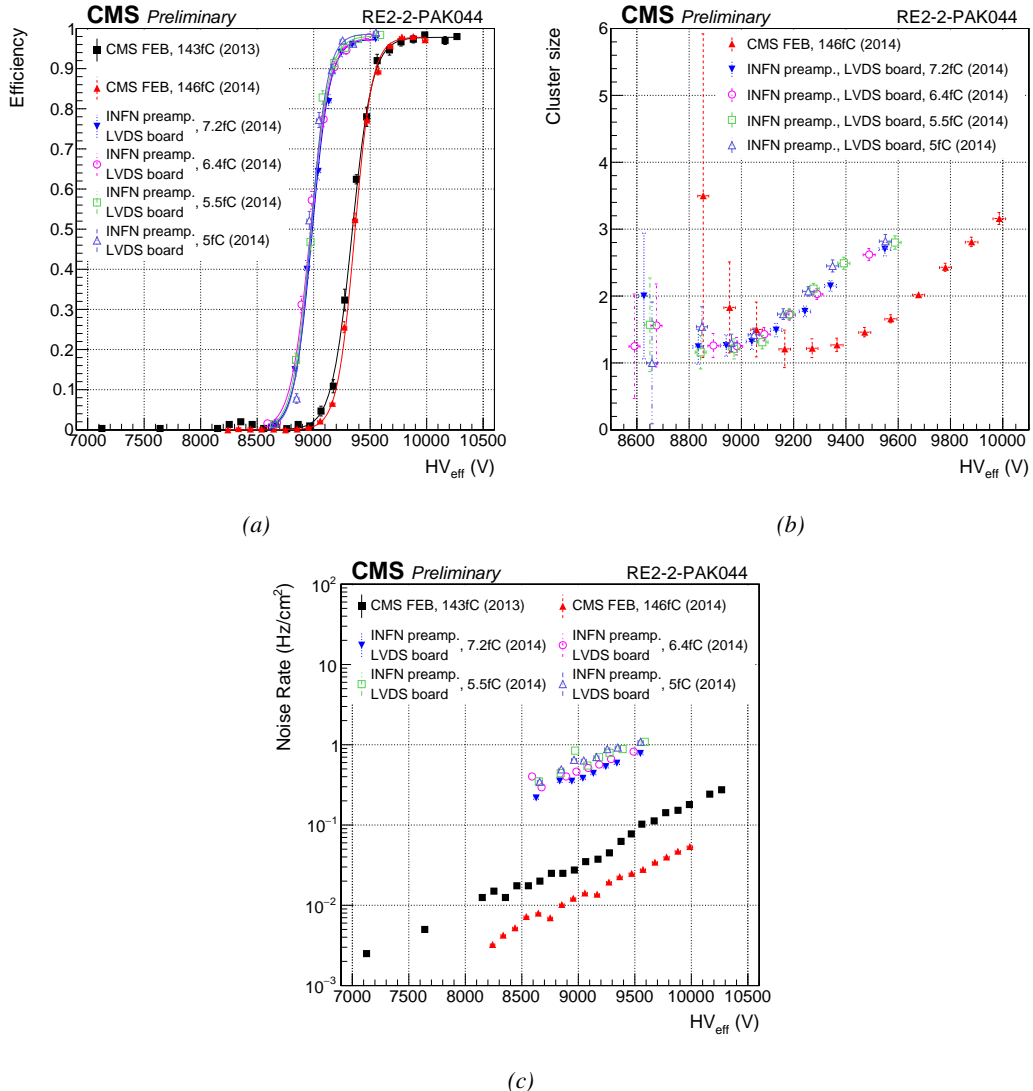


Figure 6.16: Efficiency (Figure 6.16a), cluster size (Figure 6.16b) and noise rate per unit area (Figure 6.16c) of the CMS RE2-2 detector tested with the standard CMS FEBs (black and red) and with the INFN preamplifier mounted onto the CMS FEB at different thresholds (blue, pink, green and purple).

Data	ϵ_{max}	$\lambda \cdot 10^{-2} \text{ V}^{-1}$	$HV_{50} (\text{V})$	ϵ_{WP}	$HV_{WP} (\text{V})$
CMS FEB, 143fC (2013)	0.978 ± 0.004	1.12 ± 0.07	9339 ± 11	0.97 ± 0.01	9752 ± 27
CMS FEB, 146fC (2014)	0.978 ± 0.003	1.30 ± 0.06	9364 ± 9	0.97 ± 0.01	9740 ± 19
INFN/CMS FEB, 7.2fC (2014)	0.973 ± 0.006	1.26 ± 0.09	8985 ± 10	0.97 ± 0.01	9368 ± 26
INFN/CMS FEB, 6.4fC (2014)	0.978 ± 0.007	1.16 ± 0.08	8969 ± 11	0.97 ± 0.01	9372 ± 28
INFN/CMS FEB, 5.5fC (2014)	0.981 ± 0.005	1.26 ± 0.09	8973 ± 12	0.97 ± 0.01	9357 ± 28
INFN/CMS FEB, 5fC (2014)	0.987 ± 0.004	1.37 ± 0.10	8976 ± 12	0.98 ± 0.01	9342 ± 28

Table 6.2: Results of the sigmoid fit (Formula 3.24) performed on the data presented in Figure 6.16a. The working point and its corresponding efficiency are computed using Formulas 3.24 and 3.25.

In addition to the tests performed on the electronics with the CMS RPC, the electronics also have been tested on a gRPC designed in Ghent. The gRPC used for this experiment is described in Figure 6.17. The detector, showed on Figure 6.18, uses a double-gap layout with float glass electrodes of 1.1 mm and a gas gap of 1.2 mm. The electrodes themselves are made out of four pieces of glass glued together. Such a design was studied for high-rate detection purposes and aimed to serve as a proof of concept for RPCs built using small pieces assembled together to produce a larger detection area. Indeed, in the context of R&D in the field of high-rate RPCs, most low resistivity materials are custom made doped glass or ceramics plates. These materials can't be produced in large areas as they are not manufactured on a large enough scale. Thus, building large detectors can imply using such methods.

The tests involving this detector were conducted in 2015 with the setup described by Figure 6.19. The photomultipliers used to trigger the data taking were a little larger than the detector and the strips themselves. Similarly to the case of the GIF experiment described in Section 5.2.2 of Chapter 5, it has been necessary to evaluate the geometrical acceptance of the setup to detect cosmic muons. This way, a C++ Monte Carlo simulation has been written using the dimensions of the experimental setup. By running 1000 simulations in which a million muons were generated in a source plane much larger than the experimental setup itself to reach high zenith angles, the geometrical acceptance was measured to be (0.9835 ± 0.0014) . This factor has then been used to correct the measured efficiency of the detector.

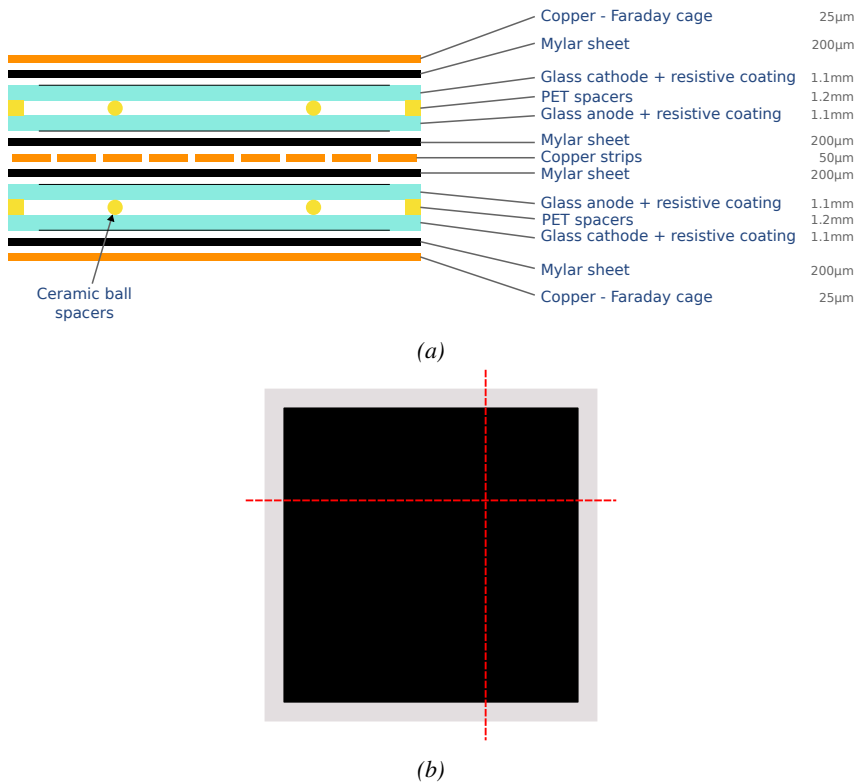


Figure 6.17: The glass RPC developed by Ghent uses a double-gap design (Figure 6.17a). The electrodes are made of four pieces of float glass glued into a single plate (Figure 6.17b). Indeed a gluing technique has been investigated as most new low resistivity materials foreseen for RPCs of the new generation are not available in large areas.

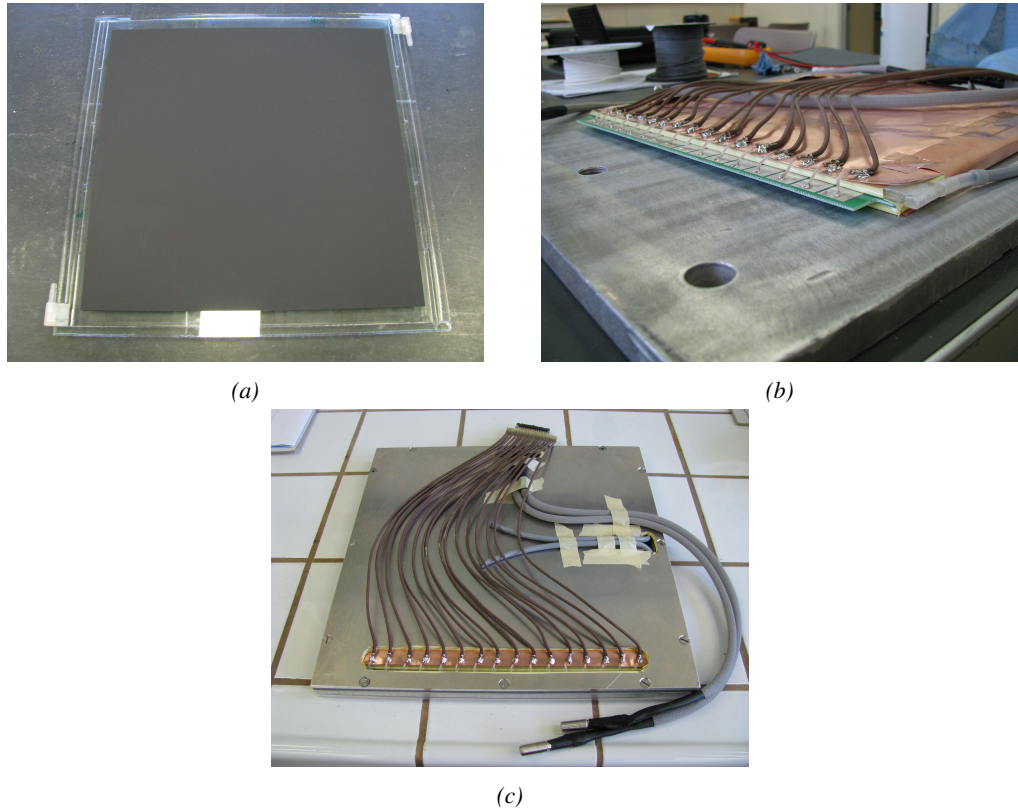


Figure 6.18: Figure 6.18a: A gap used to conceive the gRPC tested at CERN. Figure 6.18b: Both gaps with their read-out panel are placed into a faraday made out of copper. Figure 6.18c: The faraday cage containing the double-gap gRPC is finally placed into its aluminium case.

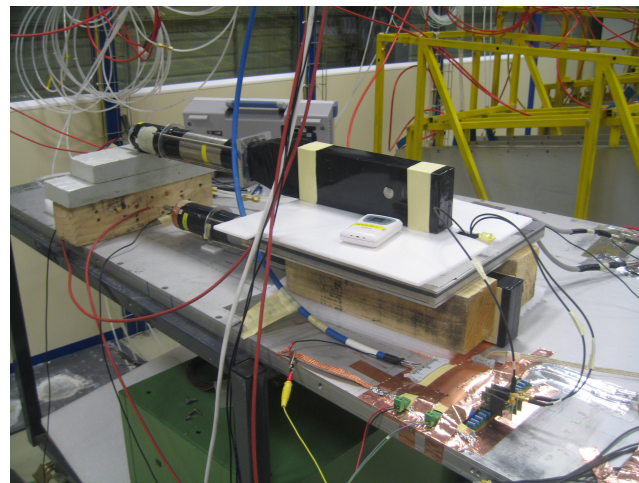


Figure 6.19: Experimental setup used to test the INFN preamplifier mounted on the CMS like FEB with the glass RPC build by Ghent.

4017 Thanks to the activities ongoing for the preparation of the CMS RPC experiment taking place
 4018 at GIF++ and detailed in Chapter 5, a first prototype of DAQ software was available to automate
 4019 the data tacking process. Thanks to this early version of the software, the pulse processing was
 4020 made more simple. The three channels connected to the preamplifiers were sent directly into a
 4021 V1190A TDC manufactured by CAEN. The trigger was provided by the same trigger pulse process-
 4022 ing described in Figure 6.15. The output of the coincidence of both scintillators was sent into the
 4023 ***TRIGGER*** input of the TDC. The communication with the computer was done thanks to a V1718
 4024 module. More details on the DAQ can be found in Appendix A. Contrary to the data now collected
 4025 at GIF++, the output of the first DAQ script consisted in a simple text file using a format described
 4026 in Source Code 6.1. The analysis is then performed using a loop through the data file.

```
4027   Evt0      nHits
  ChHit1    THit1
  ChHit2    THit2
  ChHit3    THit3
  ChHit4    THit4
  ChHit5    THit5
...
Evt1      nHits
ChHit1    THit1
ChHit2    THit2
ChHit3    THit3
...
```

4028 *Source Code 6.1: Description of the format used to store the data collected during the experiment aiming at
 testing the INFN electronics with a gRPC built by Ghent. For each trigger received in the TDC module, an
 event is created. A first line containing two columns is written in the output file with the event number `EvtX`
 and the recorded number of hits `nHits`. This line is directly followed by the list of hits in each channel `ChHitX`
 and their corresponding time stamp `THitX` organized into two columns.*

4029 The results of the experiment with the gRPC are provided in Figure 6.20 and Table 6.3. The
 4030 efficiency of the detector reaches 95% at working voltage, indicating that such a detector using
 4031 electrodes composed of several glued pieces can be an option for the future of RPC technologies.
 4032 The benefits of the preamplifiers is once again visible through the huge efficiency shift towards lower
 4033 voltages. The shift reaches almost 470 V for thresholds lower than 6 fC.
 4034 The cluster size also shows a shift but its value suddenly decreases after 5.4 kV. After a rise above 2,
 4035 the cluster size drops when the detector reaches the plateau. A first idea to explain this phenomenon
 4036 would be to check the cluster algorithm to make sure that it is not biased and does not introduce
 4037 a fake split of the clusters due to arbitrarily strict selection rules. Clusters are always made of
 4038 neighbour strips getting a hit within a certain time window. In the algorithm written to analyse
 4039 the data, it is required for the maximum time difference between the earliest hit and the latest hit
 4040 in a cluster to be smaller than 10 ns. Physically, assuming of drift velocity of the electrons in the
 4041 gas of the order of 0.1 mm/ns [286], the growth of an avalanche only takes a few ns. This effect
 4042 is visible in Figure 6.21a in which the maximum time difference has been artificially increased to
 4043 300 ns. The peak reaveals that the avalanches are not expected to grow over a time period longer than
 4044 10 ns. No peak emerges at time differences longer than 10 ns indicating that the choice of a short
 4045 time development within the algorithm was justified. This conclusion is supported by Figure 6.21b
 4046 in which the evolution of the reconstructed cluster size with increasing maximum time difference
 4047 shows no effect.

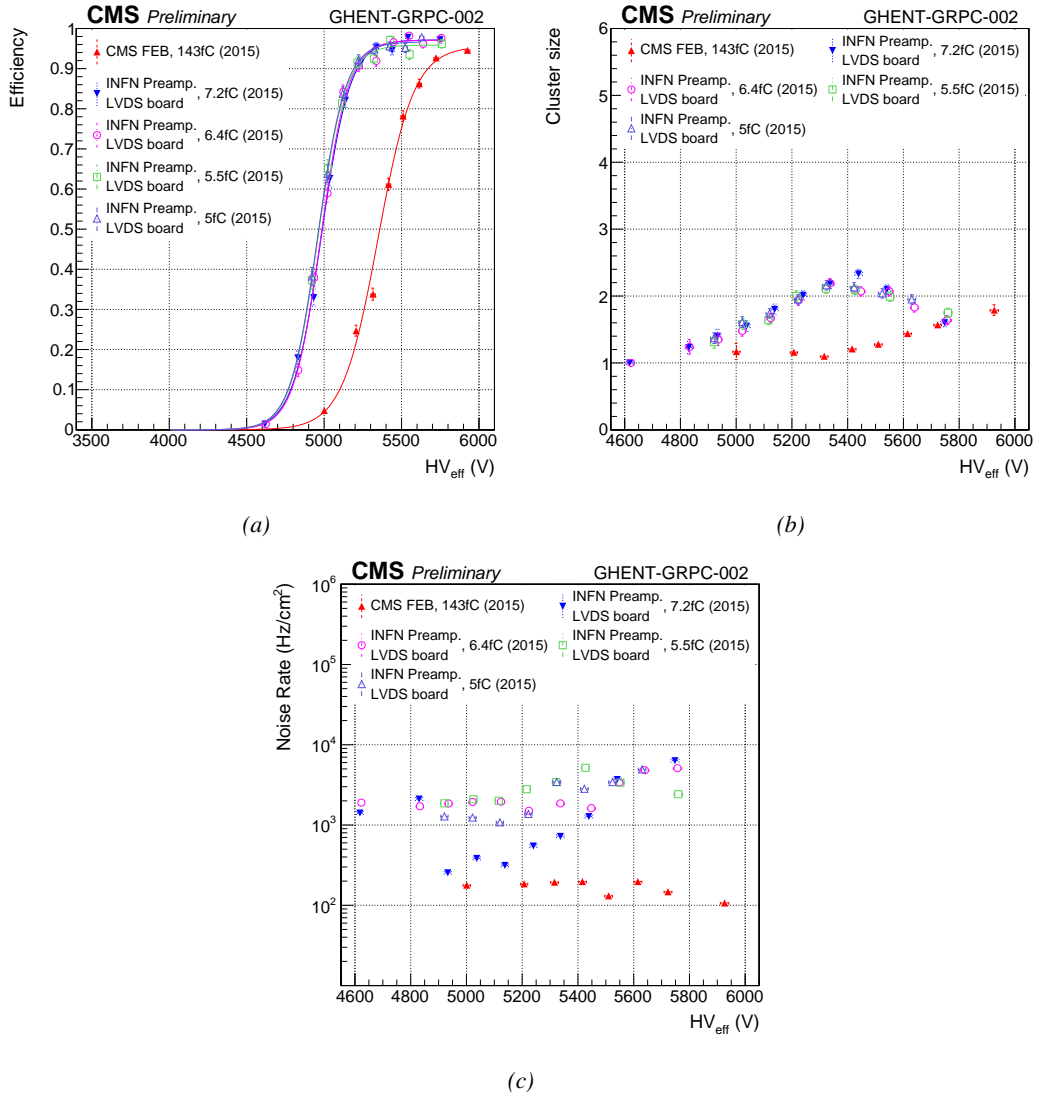


Figure 6.20: Efficiency (Figure 6.20a), cluster size (Figure 6.20b) and noise rate per unit area (Figure 6.20c) of the Ghent gRPC detector tested with the standard CMS FEBs (red) and with the INFN preamplifier mounted onto the CMS FEB at different thresholds (blue, pink, green and purple).

Data	ϵ_{max}	$\lambda \cdot 10^{-2} \text{ V}^{-1}$	$HV_{50} (\text{V})$	ϵ_{WP}	$HV_{WP} (\text{V})$
CMS FEB, 143fC (2015)	0.956 ± 0.007	0.86 ± 0.04	5349 ± 8	0.94 ± 0.01	5839 ± 23
INFN/CMS FEB, 7.2fC (2015)	0.972 ± 0.006	1.09 ± 0.06	4983 ± 8	0.96 ± 0.01	5403 ± 22
INFN/CMS FEB, 6.4fC (2015)	0.971 ± 0.005	1.13 ± 0.06	4981 ± 8	0.96 ± 0.01	5391 ± 22
INFN/CMS FEB, 5.5fC (2015)	0.959 ± 0.006	1.13 ± 0.11	4960 ± 11	0.95 ± 0.02	5371 ± 37
INFN/CMS FEB, 5fC (2015)	0.967 ± 0.006	1.12 ± 0.11	4959 ± 11	0.96 ± 0.02	5371 ± 38

Table 6.3: Results of the sigmoid fit (Formula 3.24) performed on the data presented in Figure 6.20a. The working point and its corresponding efficiency are computed using Formulas 3.24 and 3.25.

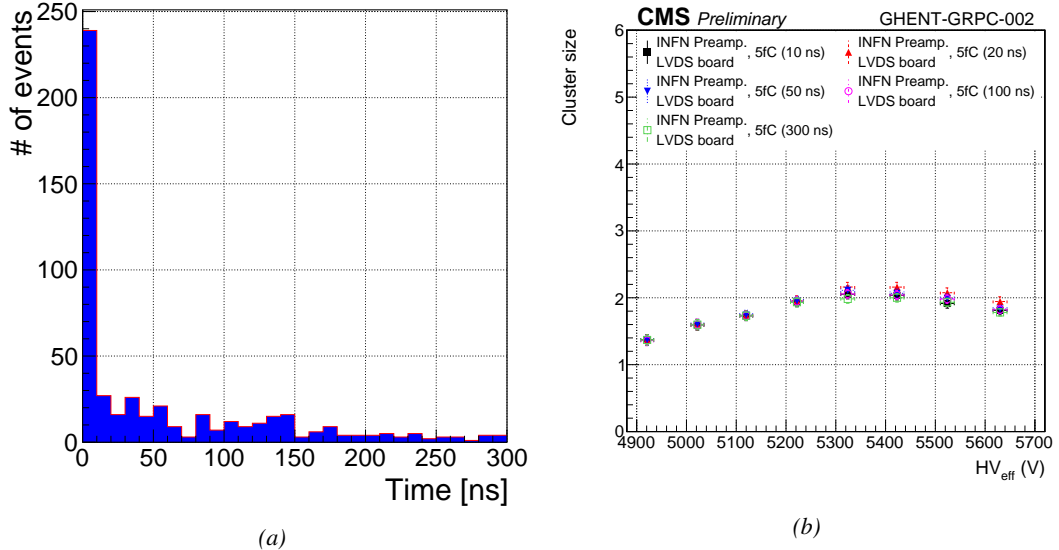


Figure 6.21: Figure 6.21a: Time difference between the first and last hit composing a cluster in the gRPC. The maximum time difference is set to 300 ns. Figure 6.21b: Variation of the reconstructed average cluster size as a function of the time constraint used in the algorithm.

4048 Due to the available number of channels, the cluster size is limited to 3. It is reasonable to
 4049 assume that this only is the cause of the fall of cluster size beyond 5.4 kV. Indeed looking closely at
 4050 both Figure 6.22 and Figure 6.23, the link between increasing HV and decreasing cluster size can be
 4051 understood. On the one hand, Figure 6.22 indicates that the cluster size features at first a maximum
 4052 at 1. The maximum moves then from 1 to 3 over the points at 5120 V, 5222 V and 5324 V. Then over
 4053 the last three voltage points, the bin at 2 drops to the profit of the bin at 1, the bin at 3 staying more
 4054 or less stable. On the other hand, Figure 6.23 provides us more information about the localisation of
 4055 the clusters among the three read-out strips. At the lowest two voltages, most of the data is contained
 4056 in the central strip. At 5120 V, the highest bin is the one corresponding to the central strip with a
 4057 cluster size of 1. Already at 5222 V, the balance changes towards the central strip with 3 strips in
 4058 the clusters. At 5324 V, even more events happen with clusters of all 3 strips while the events with
 4059 a single hit in the side strips starts to increase. The number of events with cluster made of all 3
 4060 strips will not vary much anymore while the number of events with clusters made of 2 strips will
 4061 decrease and the single hits in the side strips will continue rising. This information indicates that
 4062 the avalanches in the gap start to get stronger. Indeed, the increase of the events containing single
 4063 hits mainly increases on the side strips points to an intensification of the avalanche gain on the strip
 4064 adjacent to the three channels connected to the read-out setup. Only a single hit is read-out while
 4065 in reality this was the contribution of bigger avalanches. The events with clusters of size 2 tend to
 4066 decrease due to the stronger gain that should normally be triggering wider avalanches. The cluster
 4067 size distribution of Figure 6.22 gives the impression that the distribution is moving towards higher
 4068 values but the geometrical limitation of the system due to the very low number of channels makes it
 4069 impossible to measure.

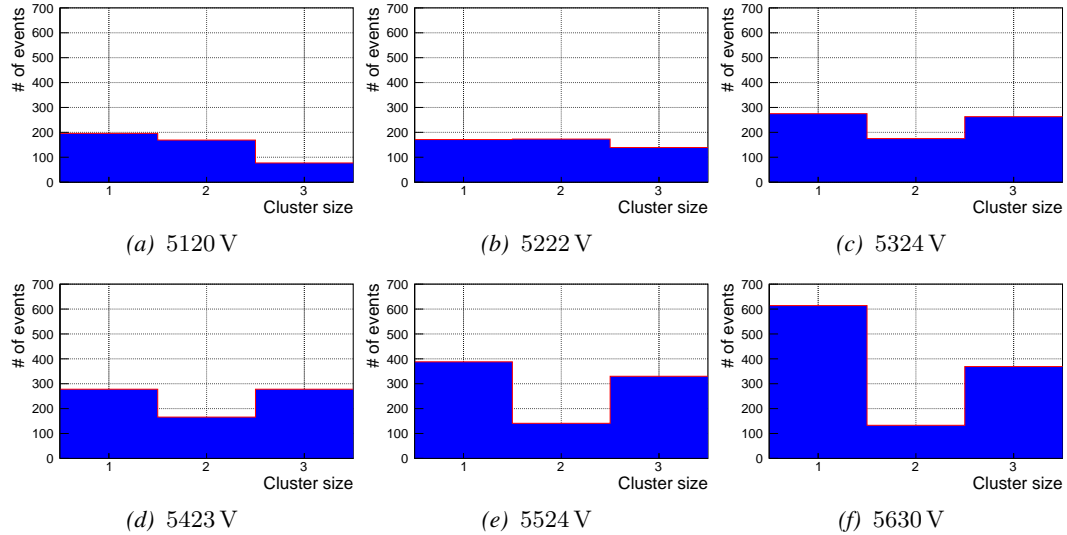


Figure 6.22: Evolution of the cluster size distribution with increasing voltage for the gRPC tested with the INFN preamplifiers using a threshold of 5 fC.

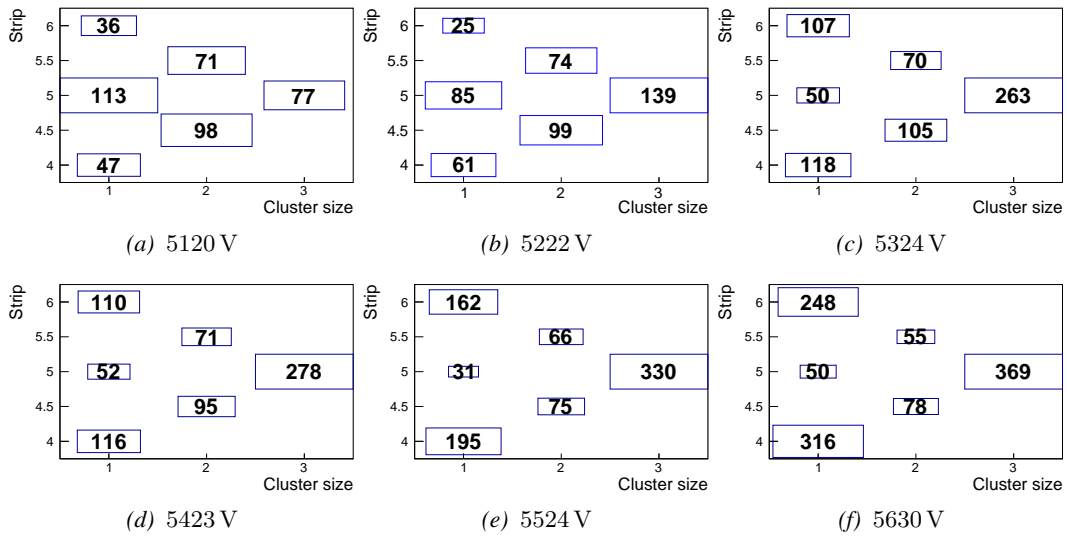


Figure 6.23: Map of the cluster size distribution as a function of the cluster position with increasing voltage for the gRPC tested with the INFN preamplifiers using a threshold of 5 fC.

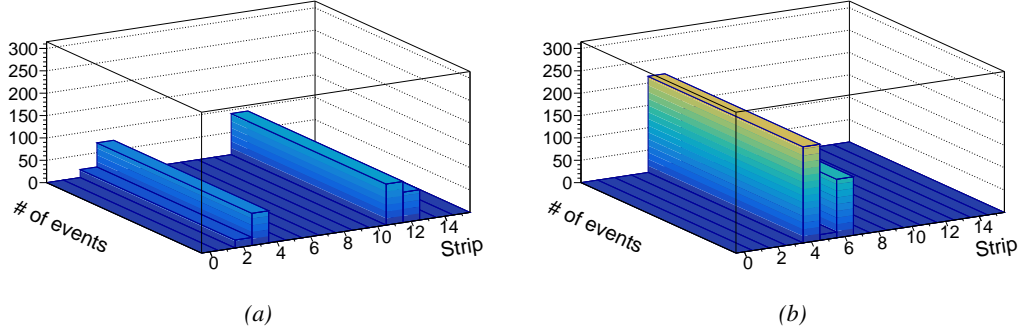


Figure 6.24: Noise profile measured in the glass RPC built by Ghent tested with the standard CMS FEB (Figure 6.24a) and the INFN preamplifiers mounted on a CMS-like FEB (Figure 6.24b).

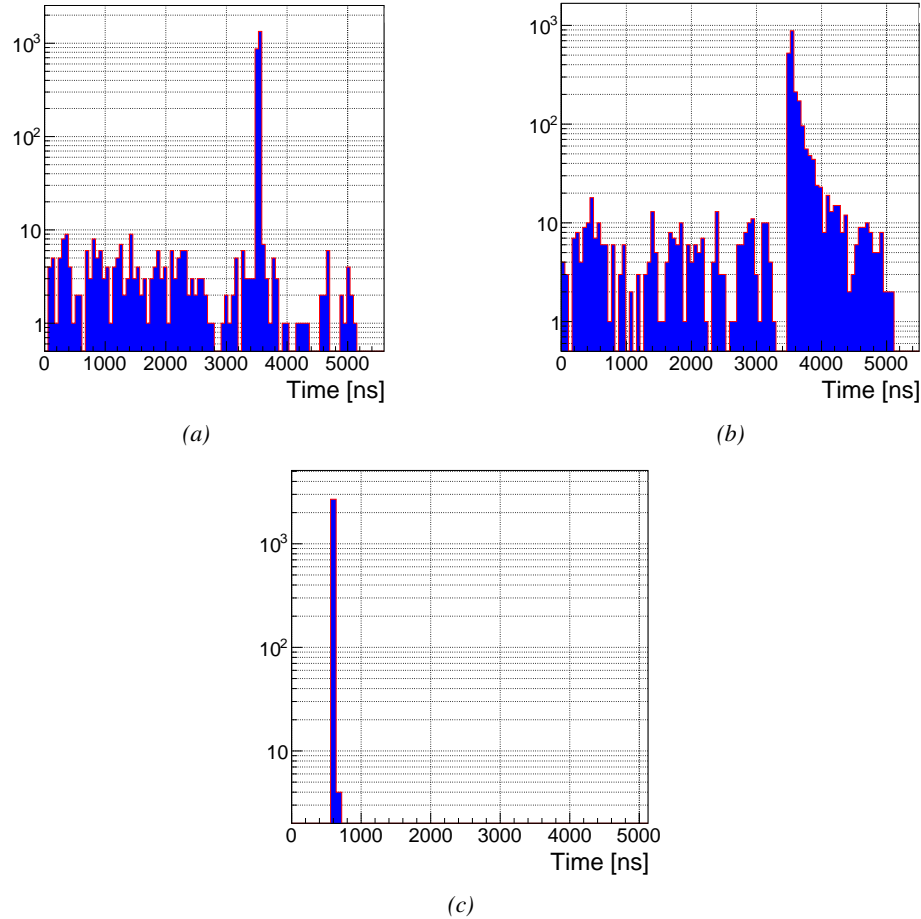


Figure 6.25: The arrival time of the hits recorded in the gRPC tested with the CMS FEB (Figure 6.25a) and with the INFN preamplifiers (Figure 6.25b), and recorded in the CMS RE2 RPC tested with the INFN preamplifiers (Figure 6.25c).

Eventhough the performance of the detector are promising, the results concerning the noise rate per unit area seem to indicate that the detector and its combination with the electronics in the case of this experiment produces very high levels of noise, if compared to the noise measured in the RE4 detector. With each type of electronics, the noise doesn't indicate a clear correlation with increasing voltage. The hypothesis at this stage would be that the noise is not created inside of the gas volume by avalanches triggered along the glueing lines, where the electric field could be abruptly pertubated. It would rather come from the read-out channel itself, and from its connection to the electronics. Indeed, looking at the noise profile measured in the detector and presented in Figure 6.24a, it is clear that the noise is localised in two areas corresponding to the HV connectors in the case of the HV scan performed with the CMS FEB. Moreover, contrary to the very careful work performed on the RE2 chamber to match the impedance of the strips with the read-out cables connected to the board on which the INFN preamplifiers are mounted, no matching was done on the gRPC due to a lack of time. The noise measured in the tested three channels is showed in Figure 6.24b. This region of the detector doesn't correpond to the HV connectors according to Figure 6.24a. Nevertheless, the number of hits counted in the detector is much higher than in the CMS FEB case. Looking more carefully to Figure 6.25 presenting the hit time profile in both cases together with the time profile of the CMS RE2-2 detector tested with INFN preamplifiers, it is clear that the detector is noisier. Also, the reflections due to the impedance mismatch is clearly visible in Figure 6.25b.

6.2.3 HARDROC 2 based RPC read-out

The HAdronic RPC Digital Read-Out Chip (HARDROC) ASIC, as its name suggests, has been developped for RPC applications and in particular for the read-out RPCs of the SDHCAL that is being studied in the perspective of the International Linear Collider (ILC). The SDHCAL detectors are required to have a high granularity compared to the CMS RPCs and hence, they use 1 cm^2 read-out pads instead of strips. This choice results in a huge number of channels. The ASIC is mounted directly on the read-out pannel for compactness as can be seen in Figure 6.26a and feature three thresholds to provide a semi-digital information.



Figure 6.26: Experimental setups used to test the HARDROC2 electronics with a CMS RE4-3 gap (Figure 6.26a) and a gRPC gap built in Ghent (Figure 6.26b).

The PETIROC that inspired the CMS RPCROC uses a similar technology than the one developed for the HARDROC and is manufactured by the same company. It is safe to conclude that the preliminary results obtained with the HARDROC electronics constitute a strong indication on

4099 the potential performance of a FEB developed specifically for CMS detectors. The leading institute
 4100 in the development of the SDHCAL based on single-gap glass RPCs (gRPCs) is the Institut de
 4101 Physique Nucléaire de Lyon (IPNL) which also played a great role in developing iRPCs for CMS.



4113 *Figure 6.27: HARDROC2 control chip with*
 4114 *its "Mezzanine" used to collect the data*
 4115 *from the different HARDROC ASICs and*
 4116 *communicate with the computer. On top of*
 4117 *the picture, the trigger is brought by a coax-*
 4118 *ial cable. The connection with the computer*
 4119 *is assured by both the USB cables.*

A read-out pannel using the HARDROC 2 technology was lended by this institute and was tested onto a CMS RPC. Contrary to the tests with the INFN preamplifiers that were made using an RE2-2 CMS RPC built in 2007 for the second endcap disk of CMS, the choice was made to use an RE4-3 detector built during LS1 to equip the fourth endcap. Indeed, the pannel can't be sandwiched between two RPC gaps due to the embedded electronics and a single CMS RPC gap was used. At the time of this experiment, only RE4-3 gaps were available and the choice was made to change detector with respect to the previous series of tests conducted on the INFN preamplifiers. As for the INFN preamplifiers, the pannel has been tested on the gRPC built by UGent. The gRPC being smaller than the HARDROC read-out that was used for the experiment but thanks to the 2D read-out using pads, this was not a problem for the data acquisition.

4120 Once again, the experiment was conducted in the
 4121 CMS RPC assembly laboratory at CERN and the setups are shown in Figure 6.26. The read-out
 4122 panel is placed directly on top of the gaps and pressed against the detector surface thanks to weights.
 4123 The same PMTs are used to provide a trigger to the data acquisition. In the particular case of the
 4124 HARDROC 2 electronics, the output signal does not correspond to the LVDS signals provided by
 4125 the CMS FEB. Moreover, there would be more than 1500 channels to constantly monitor and unfor-
 4126 tunately, there would not be enough VME TDC modules to use with the DAQ software designed for
 4127 the experiment involving the INFN preamplifiers. Nevertheless, a custom-made DAQ software was
 4128 designed by the members of IPNL's team to read-out the electronics through the chip presented in
 4129 Figure 6.27. The data is stored in the buffer of the ASIC continuously and dumped into the computer
 4130 when a trigger signal is received.

4131 The results of the tests conducted with the HARDROC 2 on a CMS gap are presented in Fig-
 4132 ure 6.28 and Table 6.4. These results can hardly be compared to what was measured with the INFN
 4133 preamplifiers as the detector was not tested using the single-gap mode. The tested thresholds are high
 4134 compared to the ones displayed by the INFN preamplifiers and are of the order of magnitude of the
 4135 current CMS FEB. Nevertheless, the performance of the detector equipped with this read-out pannel
 4136 is measured to be better. Indeed, a shift of 400 to 500 V is observed at thresholds ranging from 230
 4137 to 121.4 fC. *This could be explained by the difference in read-out channel areas of both read-out*
 4138 *panels. Indeed, in the case of the standard CMS RPC, the read-out panel consists in relatively large*
 4139 *trapezoidal strips when the read-out of the HARDROC 2 is composed of 1 cm² pads. Due to the*
 4140 *cross-talk between adjacent channels, the charge produced by a growing avalanche is spread over a*
 4141 *larger surface in the case of the standard CMS RPC, leading to a smaller signal relative to the pads.*
 4142 **[This is only I idea to explain this phenomenon for now. It needs cross check. If approved, I**
 4143 **would need to quantify the expected difference.]**

4144 The cluster size is provided for information as a direct comparison of the cluster size measured with
 4145 1 cm² pads and long copper strips with width of a few cm is not possible. The measured cluster size
 4146 at working voltage with the CMS FEB is consistent with what would be expected of a single-gap
 4147 RPC. Indeed, the usage of two gaps in an OR system allows for a stronger overall gain and hence,

the cluster size is greater. A more precise estimation of the charge spread inside of the gap is obtained using pads instead of strips. At working voltage, an avalanche is detected within less than two pads on average. An extra information could be used to further improve the spatial resolution of the detector. Indeed, as stated in the introduction of the Section, the HARDROC 2 is a semi-digital electronics and features three threshold levels. Tuning these thresholds would lead to an approximation of the induced charge profile over the neighbouring pads. A gaussian fit over the digitized distribution would give an estimation of the position of the avalanche center.

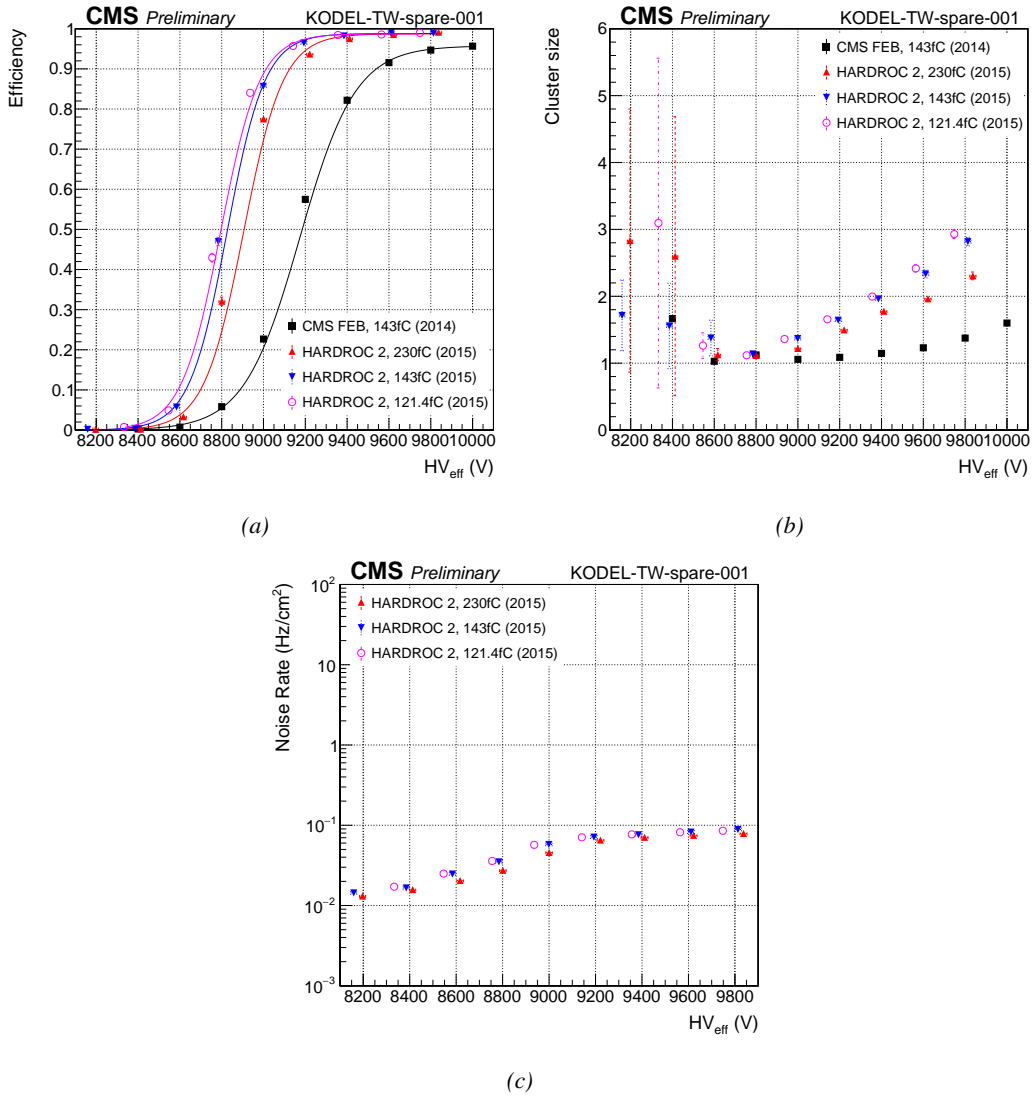


Figure 6.28: Efficiency (Figure 6.28a), cluster size (Figure 6.28b) and noise rate per unit area (Figure 6.28c) of the CMS RE4-3 detector tested in single gap mode with the standard CMS FEBs (black) and with the HARDROC 2 readout panel at different thresholds (red, blue and pink).

Data	ϵ_{max}	$\lambda \cdot 10^{-2} \text{ V}^{-1}$	$HV_{50} (\text{V})$	ϵ_{WP}	$HV_{WP} (\text{V})$
CMS FEB, 143fC (2014)	0.958 ± 0.000	0.75 ± 0.00	9174 ± 1	0.94 ± 0.00	9716 ± 2
HARDROC 2, 230fC (2015)	0.987 ± 0.002	1.06 ± 0.04	8905 ± 8	0.98 ± 0.01	9333 ± 17
HARDROC 2, 143fC (2015)	0.988 ± 0.001	1.10 ± 0.04	8826 ± 8	0.98 ± 0.01	9243 ± 17
HARDROC 2, 121.4fC (2015)	0.987 ± 0.001	1.07 ± 0.04	8795 ± 8	0.98 ± 0.01	9220 ± 17

Table 6.4: Results of the sigmoid fit (Formula 3.24) performed on the data presented in Figure 6.28a. The working point and its corresponding efficiency are computed using Formulas 3.24 and 3.25.

Finally, the noise measured in the electronics is of the same order of what had been measured in Figure 6.16c. It is safe to assume that the noise level in the case of a single-gap RPC is expected to be of the same order of magnitude than its double-gap counterpart as the noise mainly is electromagnetic. Figure 6.29 provides a clearer understanding of the position of the trigger PMTs and of the noise measured with the HARDROC. The noise of the electronics itself is very small and the read-out pannel is sensitive enough to measure the noise in the RPC gap. Indeed, except for a few visible hot spots, the observed noise profile corresponds perfectly to the spacer positions inside of the gap volume. The PET buttons used to maintain the uniformity of the gas volume cause noise at their proximity as they modify the local electric field.

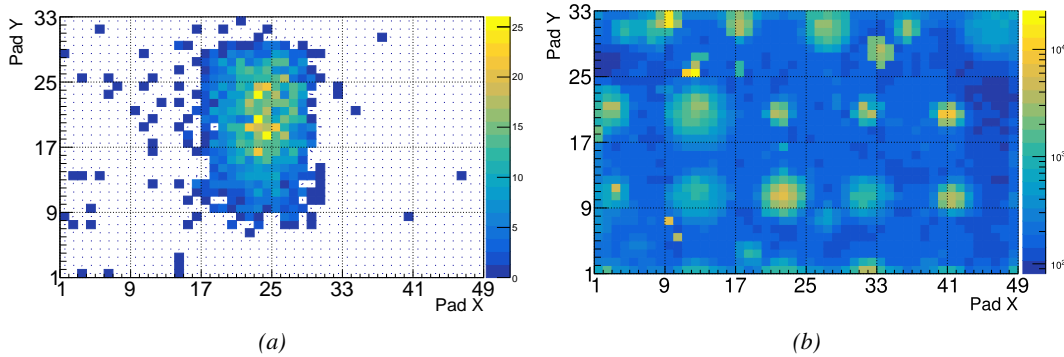


Figure 6.29: Measured muon (Figure 6.29a) and noise (Figure 6.29b) profiles in the read-out pads of the HARDROC 2 over a CMS RE4-3 gap. The inner structure of the gap and the presence of the spacers in the volume is visible.

The results of the experiment with the gRPC are provided in Figure 6.30 and Table 6.5. Unfortunately the gRPC had not been tested in single gap mode with the CMS FEB. Thus, a direct comparison is not possible as the data were not collected in similar conditions. The detector could only be tested with a single HARDROC 2 threshold setting (143 fC). As for the double-gap, the efficiency of the single-gap reaches 95% at working voltage. The working voltage is consistent with the double-gap detector operated with the CMS FEB indicating that the HARDROC is more sensitive to lower charges. The difference in efficiency rising is consistent with the use of one gap versus two in the case of the CMS FEB.

As discussed in the case of the CMS RE4-3 gap, the direct comparison of the cluster sizes is not possible. In this sense, the proximity of both results only is fortuitous. The cluster size of approximately 1.6 measured with the HARDROC 2 at working voltage is of the same order than what had previously been measured for the CMS gap indicating that at equivalent performance, the gain and hence, the induced charge could be comparable.

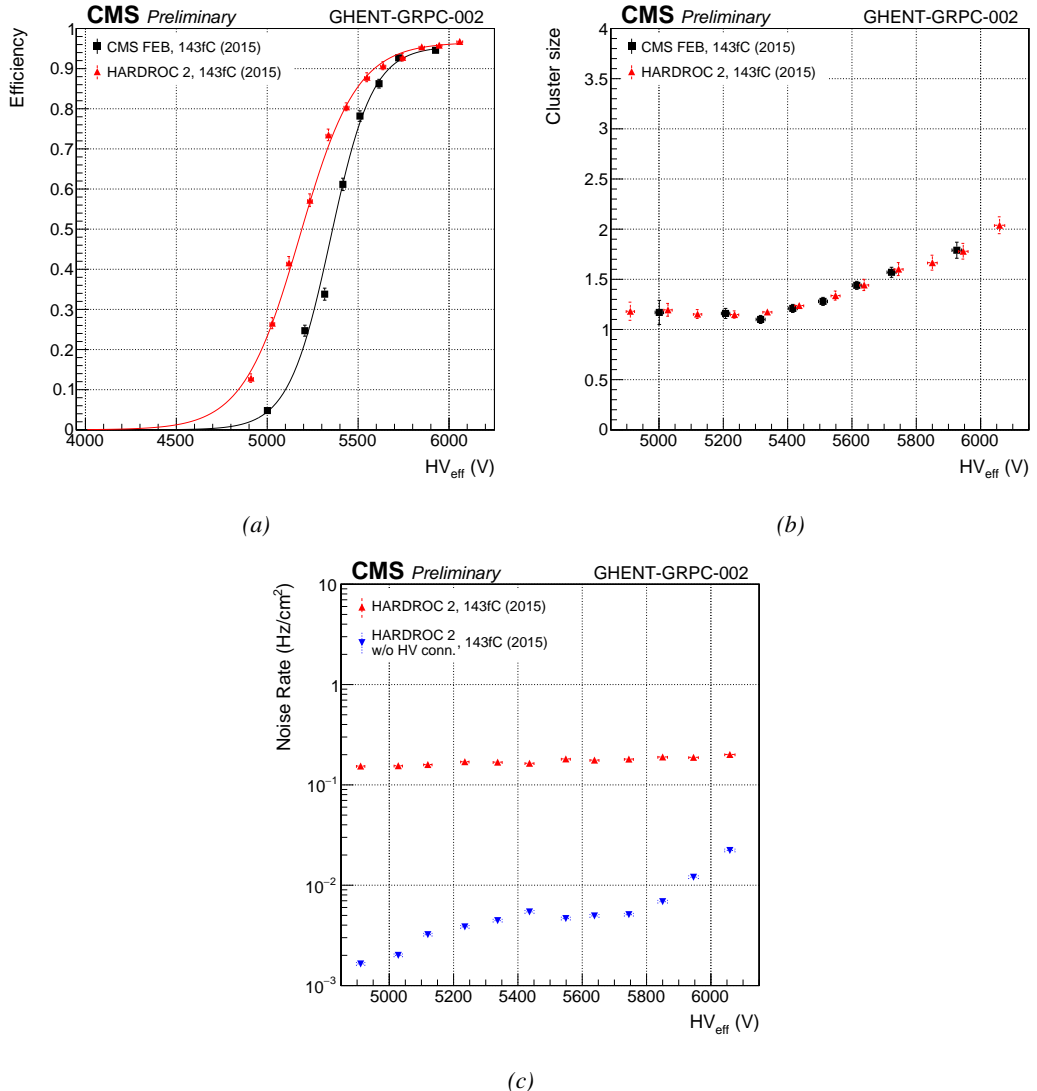


Figure 6.30: Efficiency (Figure 6.28a), cluster size (Figure 6.28b) and noise rate per unit area (Figure 6.28c) of the UGent gRPC tested in double-gap mode with the standard CMS FEBs (black) and in single-gap with the HARDROC 2 readout panel at a threshold of 143 fC (red).

Data	ϵ_{max}	$\lambda \cdot 10^{-2} \text{ V}^{-1}$	$HV_{50} (\text{V})$	ϵ_{WP}	$HV_{WP} (\text{V})$
CMS FEB, 143fC (2015)	0.956 ± 0.007	0.86 ± 0.04	5349 ± 8	0.94 ± 0.01	5839 ± 23
HARDROC 2, 143fC (2015)	0.966 ± 0.004	0.64 ± 0.02	5179 ± 7	0.95 ± 0.01	5790 ± 25

Table 6.5: Results of the sigmoid fit (Formula 3.24) performed on the data presented in Figure 6.30a. The working point and its corresponding efficiency are computed using Formulas 3.24 and 3.25.

Finally, the noise measured in the electronics seemed higher than in the case of the CMS gap. Looking closer to the noise profile provided in Figure 6.31, it can be seen that the noise measurement was affected by the HV connector. Indeed, the high noise measured in pads 41 and 42 along X and 22

to 25 along Y, corresponds exactly to the position of the HV connector on the cathode side. Contrary to the case of the CMS gap were the HV connector was far from the read-out area, the gRPC is smaller than the read-out and due to the poor grounding of the setup the electric field created by the HV connector could affect the read-out. Excluding the corresponding pads gives a much more reliable noise measurement as can be seen in Figure 6.30c. Through the noise profile, a better understanding of the gRPC uniformity can be obtained. First of all, the row corresponding to Y=16 seem consistently noisier than the neighbouring pads and could correspond to the glueing line that lies along this pad row. The noise increase along this line is not very clear though and no corresponding behaviour can be observed along the other glueing line along column X=30. But the gas volume corresponding to the largest glass plate, spreading from columns 31 to 47 along X and rows 1 to 15 clearly shows a stronger noise in its center. The detection area being small, only a few ceramic ball spacers were used to maintain the distance in between the electrodes. It is not impossible that the ball spacer located in the center of this very volume popped out. Due to the absence of a spacer, the force applied by electric field onto the electrodes could have made the distance in between the electrodes smaller and artificially increased the observed electric field, also increasing the measured noise.

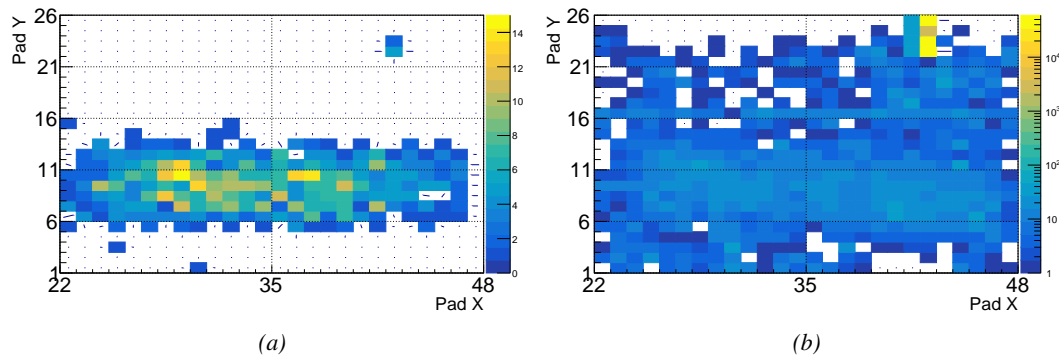


Figure 6.31: Measured muon (Figure 6.31a) and noise (Figure 6.31b) profiles in the read-out pads of the HARDROC 2 over a gRPC gap built by Ghent.

6.3 Outlook on the current FEE certification status

In this Section will be presented the ongoing certification of the CMS RPCROC and of the INFN Tor Vergata FEBs chosen as back-up solution. For reference, an iRPC has been operated without irradiation with the standard CMS FEB. It is reminded that the iRPCs that will complete the redundancy of the muon system of CMS close to the beam line are expected to suffer a background hit rate per unit area of 600 Hz/cm². Including a safety factor of 3, it is then necessary for the detectors to be certified at a minimal background hit rate of 2 kHz/cm².

6.3.1 CMS Front-End Board reference

The iRPCs that will be installed at CMS will be equipped with new Front-End Electronics. Nevertheless, in order to compare the performance of the new electronics with the standard CMS FEBs, a series of short characterization tests was carried out with an iRPC prototype. Seven strips of a read-out panel designed for a back-up scenario detector were connected to a CMS FEB. The remaining strips were connected to the ground to avoid noise. The tests were done without irradiation and using cosmic muons. Two narrow scintillators were placed on each side of the prototype to provide a trigger signal as can be seen from Figure 6.32. The tests were performed with three detection thresholds

⁴²¹⁰ of 200 mV (≈ 133 fC), 210 mV (≈ 140 fC) and 220 mV (≈ 146 fC) on the FEB discriminators. The
⁴²¹¹ LVDS output of the FEB was then read-out with a CAEN TDC.

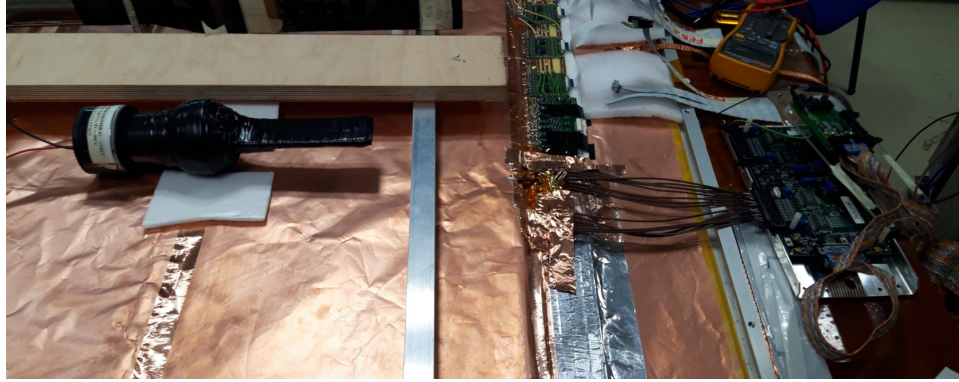


Figure 6.32: Experimental setup used to test the iRPC equipped with the standard CMS FEEs. Seven of the 96 strips are connected to the read-out channels.

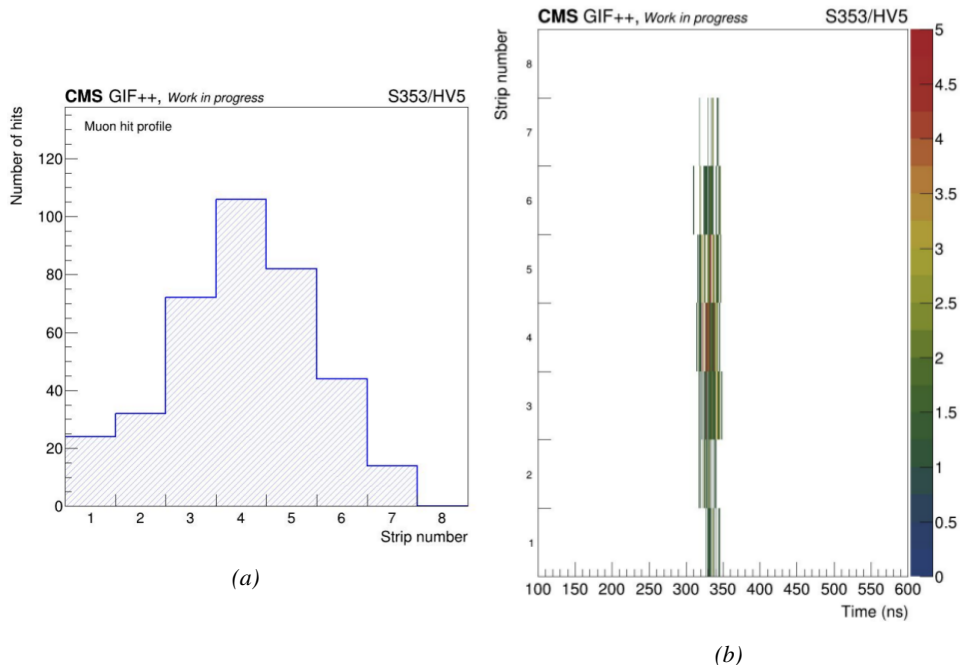


Figure 6.33: (a) Distribution of the muon hits on the seven strips connected to the standard CMS FEB. Strip 8 is connected to the ground. (b) Time distribution of the hits in the seven channels. The color scale corresponds to the number of hits per bin.

⁴²¹² The HV scans consisted of seven effective voltage steps (6800, 7000, 7100, 7200, 7300, 7400
⁴²¹³ and 7500 V) at which 100 muon triggers were requested as minimal statistics. The hit profile over the
⁴²¹⁴ connected strips as well as the time profile of the events in each channel is provided in Figure 6.33
⁴²¹⁵ for the fifth HV step (7300 HV). The area covered by the trigger is seen to be comparable than the
⁴²¹⁶ width of the seven strips. The time arrival of the hits is well confined within less than 50 ns.

The results for this kind of electronics are to be found in Figure 6.34. First of all, the efficiency at working voltage of the detector reaches 96.9% at a threshold of 146 fC, 97.0% at 140 fC and finally 96.6% at 133 fC. The efficiency does not seem to be affected by a change of threshold. The working voltage, on the other hand, is shifted towards lower effective voltage values with decreasing threshold. The values of working voltages respectively are 7552, 7473 and 7393 V. This is expected by the lower gain necessary to produce large enough avalanches. No other differences can be observed at the level of the mean muon cluster sizes, mean muon cluster multiplicity per event and noise rate per unit area. The mean muon cluster size stays of the order of 2.4 strips per cluster and the muon cluster multiplicity, which is the number of reconstructed muon clusters per event, is consistent with 1 as expected. Finally, the noise rate per unit area is below 1 Hz/cm². The results are summarized in Table 6.6.

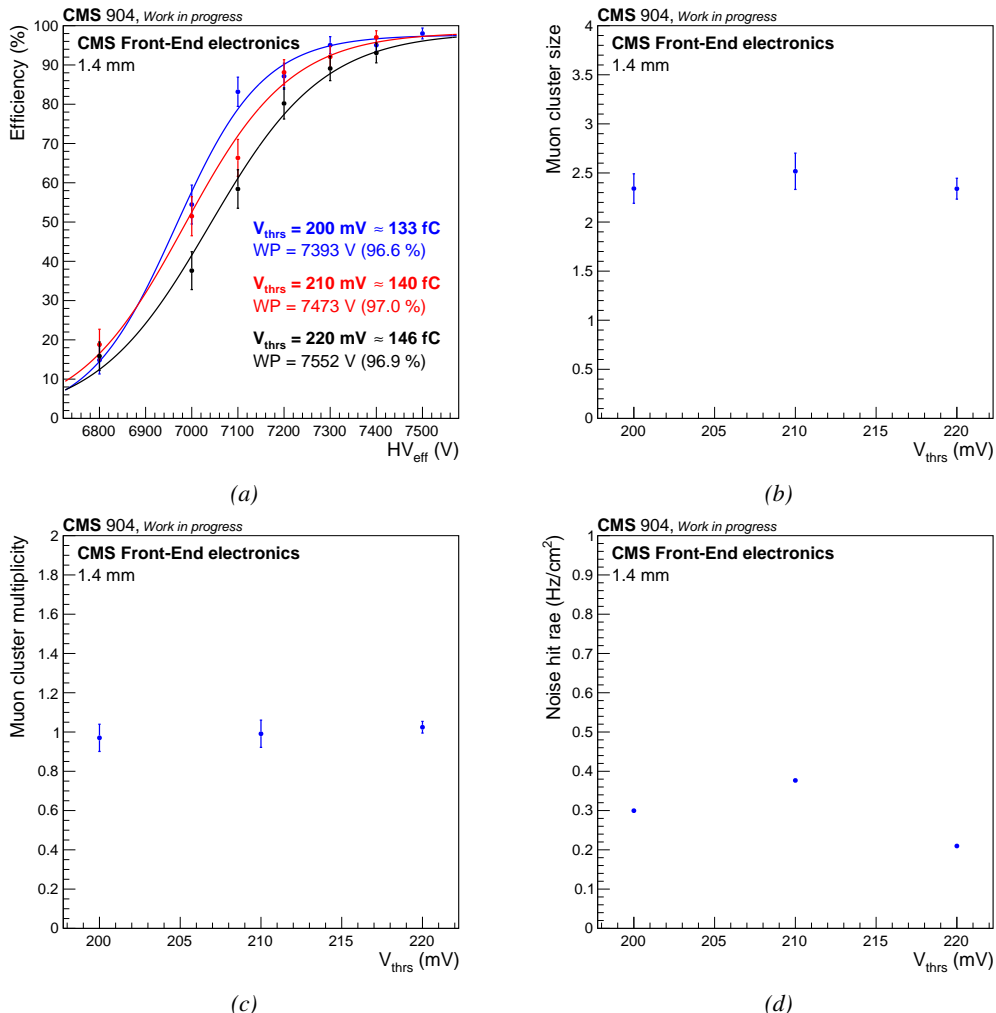


Figure 6.34: Summary of the HV scans performed on the iRPC prototype equipped with a standard CMS FEB at three detection thresholds. (a) Efficiency sigmoids. (b) Mean muon cluster size at working voltage. (c) Mean muon cluster multiplicity at working voltage. (d) Noise hit rate per unit area at working voltage.

Threshold (fC)	Working Voltage (V)	Efficiency (%)	Cluster Size	Multiplicity	Noise (Hz/cm ²)
146	7552 ± 57	96.6 ± 1.8	2.34 ± 0.11	1.02 ± 0.03	0.21
140	7473 ± 49	97.0 ± 2.5	2.52 ± 0.18	0.99 ± 0.07	0.38
133	7393 ± 45	96.9 ± 3.0	2.34 ± 0.15	0.97 ± 0.07	0.30

Table 6.6: Summary results of the iRPC operated with a standard CMS RPC FEB.

4228 6.3.2 CMS RPCROC

4229 6.3.3 INFN FEE

4230 An iRPC prototype equipped with the INFN Tor Vergata FEBs and a longitudinal read-out panel
 4231 alone was placed at the GIF++ for certification purposes. The chamber was tested for different
 4232 irradiation values.



Figure 6.35: iRPC prototype equipped with INFN Tor Vergata FEBs. The iRPC is enclosed in a spare RE1/3 case. The dimensions of the RE3/1 and RE4/1 iRPCs is in fact much smaller.

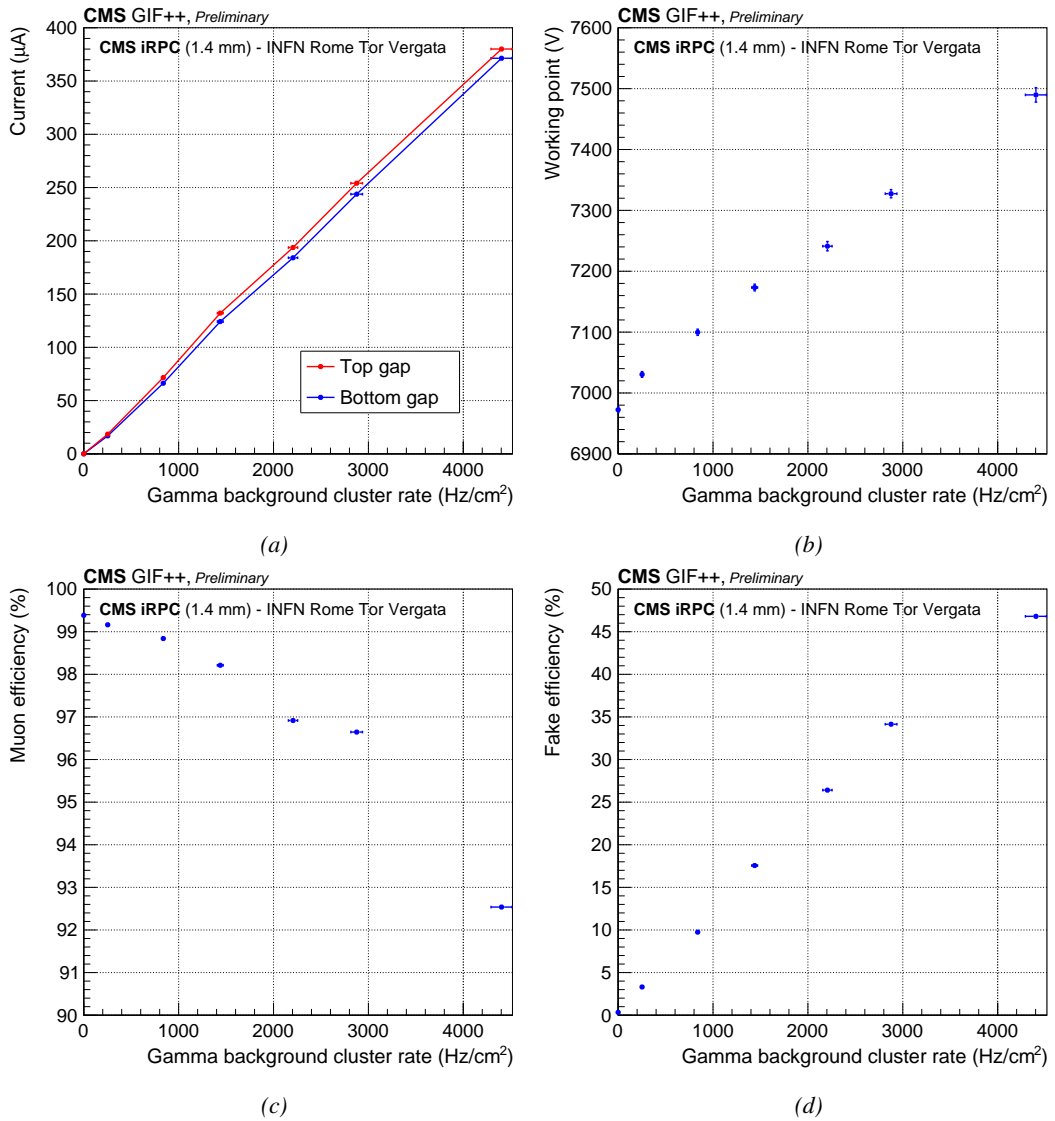


Figure 6.36

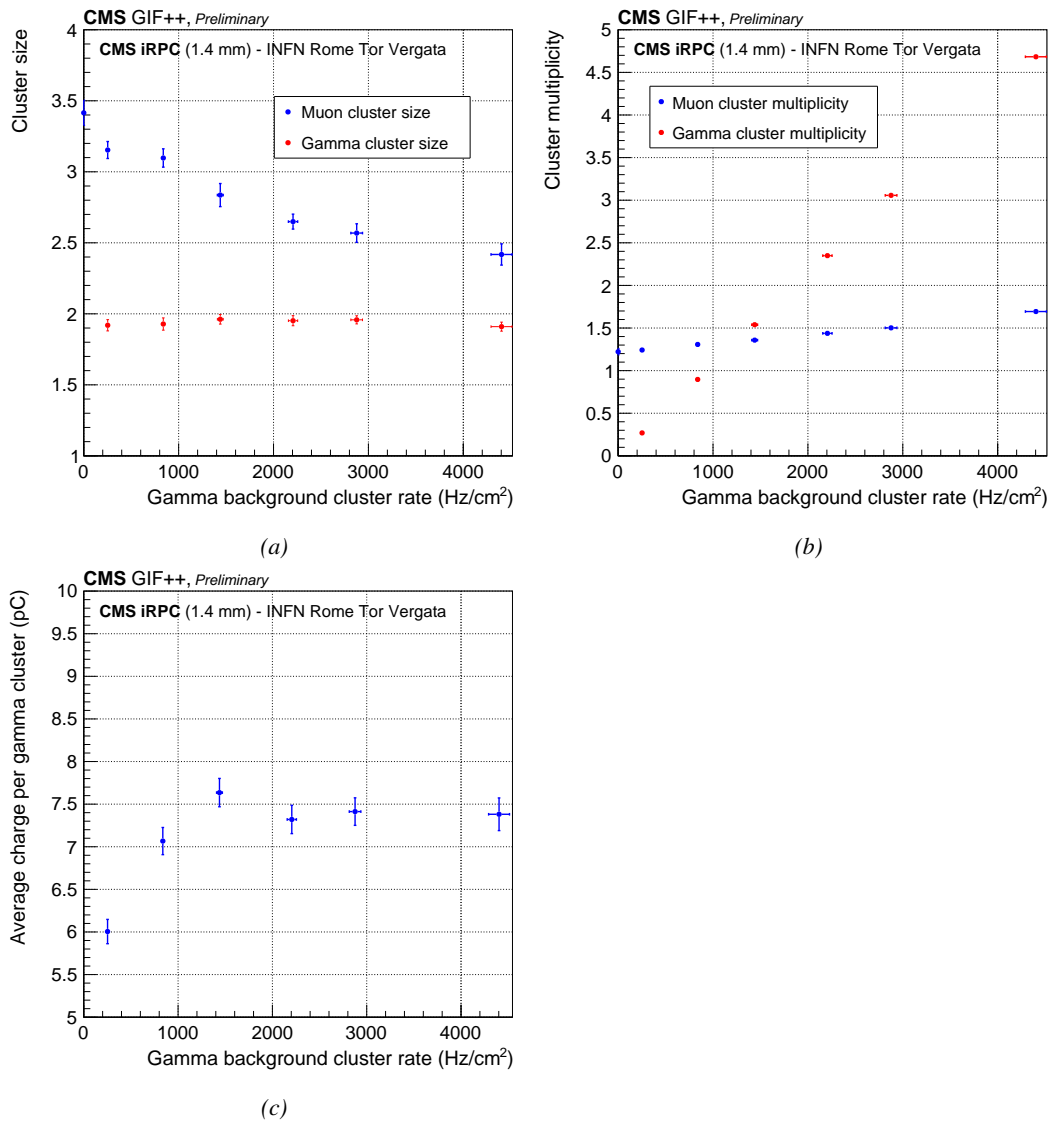


Figure 6.37